

RESEARCH ARTICLE

WILEY

Lagrangian–Eulerian multidensity topology optimization with the material point method

Yue Li^{1,2} | Xuan Li^{1,3}  | Minchen Li^{1,3} | Yixin Zhu⁴ | Bo Zhu⁵ | Chenfanfu Jiang^{1,3}

¹Computer and Information Science, University of Pennsylvania, Philadelphia, Pennsylvania, USA

²ETH Zürich, Zürich, Switzerland

³Mathematics Department, University of California, Los Angeles, Los Angeles, California, USA

⁴Computer Science Department, University of California, Los Angeles, Los Angeles, California, USA

⁵Computer Science, Dartmouth College, Hanover, New Hampshire, USA

Correspondence

Xuan Li, Mathematics Department, University of California, Los Angeles, Los Angeles, California, USA.

Email: xuan.shayne.li@gmail.com

Minchen Li, Mathematics Department, University of California, Los Angeles, Los Angeles, California, USA

Email: minchernl@gmail.com

Chenfanfu Jiang, Mathematics Department, University of California, Los Angeles, Los Angeles, California, USA

Email: chenfanfu.jiang@gmail.com

Funding information

Dartmouth College, Grant/Award Numbers: Burke Research Initiation Award, Dartmouth Neukom Institute CompX Faculty Grant; Defense Advanced Research Projects Agency, Grant/Award Number: XAI N66001-17-2-4029;

Department of Energy, Grant/Award Number: ORNL subcontract 4000171342; National Science Foundation,

Grant/Award Numbers: CCF-1813624, ECCS-2023780, IIS-1943199, MRI-19196;

Office of Naval Research, Grant/Award Numbers: ONR MURI N00014-16-12007,

ONR N00014-19-1-2153; Toyota Motor Engineering & Manufacturing North America

Abstract

In this paper, a hybrid Lagrangian–Eulerian topology optimization (LETO) method is proposed to solve the elastic force equilibrium with the Material Point Method (MPM). LETO transfers density information from freely movable Lagrangian carrier particles to a fixed set of Eulerian quadrature points. This transfer is based on a smooth radial kernel involved in the compliance objective to avoid the artificial checkerboard pattern. The quadrature points act as MPM particles embedded in a lower-resolution grid and enable a subcell multidensity resolution of intricate structures with a reduced computational cost. A quadrature-level connectivity graph-based method is adopted to avoid the artificial checkerboard issues commonly existing in multiresolution topology optimization methods. Numerical experiments are provided to demonstrate the efficacy of the proposed approach.

KEYWORDS

material point method, multidensity approach, topology optimization

1 | INTRODUCTION

Topology optimization is experiencing a rapid advance over the past few years, thanks to the collision of waves between next-generation computing infrastructure and high-performance simulation software. A surge of recent work has been creating various computing infrastructures capable of accommodating topology optimization applications with a super-scale resolution—millions to one billion of material voxels—on parallelizable data structures (e.g., References 1-3). These density-based approaches stem from the conventional Solid Isotropic Material with Penalization Method (SIMP)^{4,5} and naturally fall into Eulerian methods, owing to their geometric representation of the material evolution on a fixed grid. Level set-based methods⁶⁻¹⁰ are also Eulerian due to an implicit representation of the topology on grid nodes. On the other hand, Lagrangian geometries are increasingly attracting attention. For example, particles (e.g., in smoothed-particle hydrodynamics [SPH]¹¹) can explicitly track the structural evolution under the guidance of material derivatives. Tracking explicit meshes is also a promising direction thanks to the advent of high-performance meshing software.¹²

1.1 | Hybrid representation

Despite extensive research, Eulerian approaches have limited capability in capturing intricate structures, especially when the problem requires fine features that are hierarchical, codimensional, and can emerge from a nihil. On the other hand, Lagrangian representations suffer from a lower computational performance. Analogous to their computational physics counterparts (e.g., in computational fluid dynamics), Eulerian approaches are not naturally adaptive to subgrid features, whereas Lagrangian methods face challenges in establishing differential stencils that are geometrically symmetric and numerically accurate.

In computational physics, researchers face the same dilemma regarding the choice of data structures and the corresponding numerical stencils when simulating large-scale fluids and solids. This dilemma further triggered the invention of a bank of hybrid Lagrangian–Eulerian methods, such as Particle-In-Cell/Fluid-Implicit-Particle methods^{13,14} and Material Point Methods (MPMs),^{15,16} which are featured by an Eulerian background grid as a scratch pad and a set of Lagrangian particles to track geometry and topology. By conducting data transfers between the two representations, a hybrid Lagrangian–Eulerian scheme can typically leverage both sides' merits, enabling flexible and robust numerical solutions.^{14,15,17}

Motivated by such a design philosophy, some hybrid methods are also proposed for topology optimization. For example, the Moving Morphable Component (MMC) method¹⁸⁻²³ aims to substantially reduce the number of design variables by optimizing component-wise distributions. It represents structures by unions of superellipse level sets—low-dimensional morphable components that can move, deform, and overlap to track topology changes. The explicit geometric information also helps control the minimum length scale.²⁴ MMC can produce results with sharp features with attractive convergence and timing profiles. However, to acquire sophisticated geometry features, a large number of components, that is, design variables, is necessary. On the other hand, the Moving Node Approach (MNA)²⁵ represents the target shape with a set of mass nodes, of which the positions are optimized to search for an optimal structure. In MNA, the quadrature is a set of regularly sampled discretization nodes, on which the densities are computed according to the clustering of mass nodes. However, such an approach can lead to results with many isolated mass nodes disconnected from the main structure, which can only be cleaned up using an extra postprocessing step.

Inspired by these hybrid methods, a new hybrid Lagrangian–Eulerian topology optimization method—LETO is proposed in this paper. This new approach optimizes material distributions over a design domain by evolving a set of material carrier particles on a background Cartesian grid. With MPM applied for solving the static equilibrium, another set of particles, each carrying a temporally varying density, is evolved as a Lagrangian representation of material distribution, eliminating redundant, isolated particle blobs. The Lagrangian–Eulerian nature of the framework enables the communication between the moving particles and the fixed background MPM quadrature points by transferring the density values through interpolation functions. More specifically, as the carrier particles move and change their densities, the quadrature points' density values are updated accordingly, naturally providing subcell density resolution. As shown in the experiments, LETO tends to generate structures with rich branching fibers with low compliance.

1.2 | Topology optimization with the MPM

When applying the adjoint method on topology optimization for sensitivity analysis, elasticity simulation is required in each iteration to obtain the nodal displacements under force equilibrium given a material distribution and an external

load. A static elasticity solver can be applied since inertia effects are often ignored. While traditional topology optimization methods often use a grid-based Finite Element discretization, we adopt MPM for the static setting with the subcell resolution achieved by assigning a different density value to each quadrature particle. The static force equilibrium is further solved with a variational formulation that guarantees robustness and stability.

1.2.1 | Spatial discretization

Traditional topology optimization methods, including both density-based approaches^{4,26} and level set-based approaches,^{7,18} often apply grid-based Finite Element discretization for the static solve. In Finite Element Method (FEM), the same material density is assigned for all quadratures in every single cell. Therefore, the domain boundaries are formed with jagged finite element edges, and even plotting zero-level contour still results in jagged boundaries.²⁷ A grid with higher resolution is often required to alleviate these artifacts, which increases the computational cost.

MPM is a hybrid Lagrangian–Eulerian method widely used in different fields, for example, computer graphics,^{28,29} civil engineering,^{30,31} mechanical engineering.^{15,32–34} With the capability of handling large deformation,^{35–40} topology changes, and coupled materials, MPM has been considered as one of the top choices in various physics-based simulations, including fracture,^{29,41–45} viscoelastic, and elastoplastic solids,^{46,47} incompressible materials,^{48,49} high explosive explosion,⁵⁰ snow,^{28,51,52} granular material,^{53–56} and mixtures.^{57–59} In MPM, Lagrangian particles, which are also known as material points, are used to track quantities like mass, momentum, and deformation. On the other hand, a regular Eulerian grid is built to evaluate force and update velocity at each time step. Particle quantities are then updated from the interpolation of nodal quantities. MPM's convergence was demonstrated computationally and explained theoretically with a smooth, for example, quadratic B-spline, basis for grid solutions,⁶⁰ which was further verified with manufactured solutions.⁶¹ MPM is applied as the spatial discretization in this work. We also describe a static formulation for directly solving the force equilibrium, which allows defining quadrature-wise density per cell to take advantage of the subcell resolution. As shown in numerical experiments, LETO achieves a comparable convergence speed with lower structural compliance.

1.2.2 | Optimization and nonlinear integrators

Another long-standing challenge of topology optimization is to optimize structures undergoing large deformations, requiring a nonlinear elasticity model and the nonlinear equilibrium constraints. This has become increasingly meaningful with the increasing need for material and structural design in soft robotics,⁶² wearable devices, and even space antennas, etc. With large nonlinear deformations, the force equilibrium is more challenging to solve as it often leads to numerical instabilities, and the optimization itself will converge slower.

Numerical integration of partial differential systems can often be reformulated variationally into an optimization problem. These methods can often achieve improved robustness, accuracy, and performance by taking advantage of well-established optimization approaches. Simulation methods are increasingly applying this strategy to simulate both fluid,⁶³ and solid⁶⁴ dynamics, which often enable large time step sizes. The static solve simply corresponds to infinitely large time step size in a dynamic time-stepping point-of-view. Our method also takes advantage of optimization integrators to solve for the static equilibrium to high accuracy robustly.

For nonlinear optimization problems, Newton-type methods are often used because they can deliver quadratic convergence when the intermediate solution becomes close to the local optima. However, when the initial configuration is far from a local optimum, which is often true in static solves, Newton's method may fail to provide a proper search direction as the Hessian can be indefinite.^{65,66,67} Teran et al.⁶⁸ proposed a positive definite fix to project the Hessian to a symmetric positive definite form to guarantee that a descent direction can be found. This method is referred to as projected Newton (PN) throughout the paper and is applied in the static solve.

1.3 | Artificially stiff patterns

Traditional density-based topology optimization methods considering one degree of freedom for density per element may form checkerboard density patterns across elements. Such solutions are indeed optimal mathematically but meaningless in reality. To avoid the checkerboard pattern, filters^{4,5} were proposed to smooth the density or gradient field. These filters can be applied independent of the sensitivity analysis or encoded into the objective,³ where the latter one defines

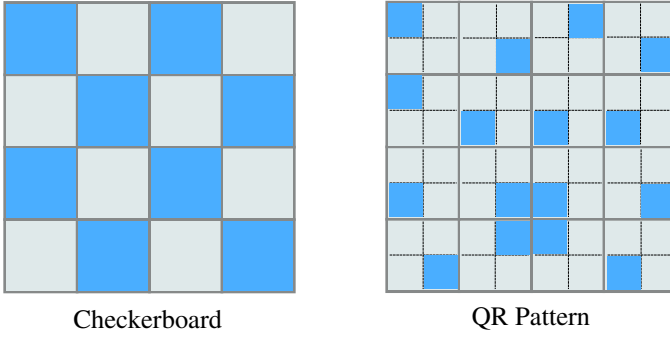


FIGURE 1 An illustration of the checkerboard issue and the QR pattern issue. In both cases, the density fields are continuous from the view of the grids

a consistent optimization problem. In this paper, the SPH kernel-based density transfer between carrier particles and quadrature points serves the same purpose and is explicitly encoded in the objective.

When multiple densities are modeled inside one element to generate higher-resolution details with a relatively low computational cost,⁶⁹ subcell-level checkerboard issues, also called the QR patterns,⁷⁰ may appear. Such artifacts happen on a subcell level where disconnected interfaces between material components may form inside one element at the quadrature level. However, from the simulation grid view, the disconnected components are connected, producing inaccurate compliance measurement at static equilibrium, which can lead to results with large compliance when tested in practice or simulated with higher resolution. An illustration of the checkerboard issue and the QR pattern issue is shown in Figure 1. Existing solutions for avoiding QR patterns include increasing the filter radius of gradient filters,⁶⁹ changing penalty power in SIMP formulation⁷⁰ and using higher-order elements.⁷¹ If applied naively, our method may encounter this kind of artifact as well if no treatment is applied since the resolution of MPM quadratures is higher than the background grid. To take advantage of the multiresolution nature of MPM while keeping the formulation simple, a graph-based narrow-band filter and a connectivity correction algorithm are developed: the set of material points is considered as a graph and only one major connected component is preserved during optimization. A secondary correction is applied after the optimization.

1.4 | Summary

In summary, a novel hybrid Lagrangian–Eulerian framework LETO is proposed for compliance-based topology optimization with MPM. The hybrid representation of the material density field enables both the flexibility of Lagrangian models and Eulerian methods' computational efficiency. The MPM discretization introduces a multidensity scheme naturally, provides a unified treatment for both linear and nonlinear topology optimization, and supports optimizing fully nonlinear compliance, enabling robust and accurate optimization of structures undergoing large deformations. A graph-based narrow-band filter and a connectivity correction algorithm are applied during and after the optimization to eliminate QR patterns. The numerical experiments show that the resulting scheme can generate subcell structures with mechanical performances that sometimes rival conventional methods at a comparable computational cost.

2 | PROBLEM STATEMENT AND METHOD OVERVIEW

2.1 | Problem statement

The general objective of compliance-based topology optimization is to seek for a material distribution ρ , a scalar field representing the material density at each point on a design domain Ω , to obtain the minimal structural compliance $c(\rho, \mathbf{u})$, or equivalently, the least strain energy $e(\rho, \mathbf{u})$, under force equilibrium between external force load \mathbf{f} and internal elasticity force $-\frac{\partial e}{\partial \mathbf{u}}$ with displacement \mathbf{u} :

$$\min_{\rho} c(\rho, \mathbf{u}) = e(\rho, \mathbf{u}) \quad \text{s.t.} \quad \begin{cases} \frac{\partial e}{\partial \mathbf{u}}(\rho, \mathbf{u}) = \mathbf{f} \\ \mathbf{D}\mathbf{u} = \mathbf{0} \\ V(\rho) \leq \hat{V}. \end{cases} \quad (1)$$

Here $\mathbf{D}\mathbf{u} = \mathbf{0}$ is the discretized Dirichlet boundary condition where \mathbf{D} selects the zero displacement nodes, $V(\rho) = \int_{\Omega_0} \rho d\mathbf{X}$ is the total volume of the structure, and \hat{V} is an upper bound specified by users to avoid trivial solutions.⁴

Usually, ρ is expected to be close to either 0 or 1 for manufacturing, which potentially makes the problem nonsmooth. The density field ρ can be discretized and further parameterized by any set of design variables. For example, the traditional SIMP method assumes that each finite element has a uniform density and directly uses cell densities as design variables. In this paper, a set of movable Lagrangian particles carried with density sources is used as design variables.

The strain energy of the material under a displacement field \mathbf{u} is defined as

$$e(\rho, \mathbf{u}) = \int_{\Omega} \Psi(\mathbf{F}) d\mathbf{X}, \quad (2)$$

where Ψ is the elastic energy density determined by the underlying constitutive model, and \mathbf{F} is the deformation gradient defined as

$$\mathbf{F} = \frac{\partial \mathbf{x}}{\partial \mathbf{X}} = \mathbf{I} + \frac{\partial \mathbf{u}}{\partial \mathbf{X}} \quad (3)$$

through the world and material space coordinates \mathbf{x} and \mathbf{X} with $\mathbf{u}(\mathbf{X}) = \mathbf{x} - \mathbf{X}$ and \mathbf{I} is the identity matrix. For linear elasticity,

$$\Psi_L(\mathbf{F}) = \mu \|\epsilon(\mathbf{F})\|^2 + \frac{\lambda}{2} \text{tr}(\epsilon(\mathbf{F}))^2, \quad (4)$$

where $\epsilon(\mathbf{F}) = \frac{1}{2}(\mathbf{F} + \mathbf{F}^T) - \mathbf{I}$ is the small strain, and the Lamé parameters μ and λ linearly relate to the Young's modulus E . However, linear elasticity is only accurate under infinitesimal deformation since rotation is also penalized, and the nonlinear stress–strain curve is not well captured. A nonlinear constitutive model should be used to model large deformation. In this paper, we adopt the neo-Hookean hyperelasticity model:

$$\Psi_{\text{NH}}(\mathbf{F}) = \frac{\mu}{2} (\text{tr}(\mathbf{F}^T \mathbf{F}) - d) - \mu \log J + \frac{\lambda}{2} (\log J)^2, \quad (5)$$

where $J = \det \mathbf{F}$, and $d = 2$ or 3 is the dimension of the problem.

The compliance objective depends on both the density ρ and the displacement \mathbf{u} , which is generally nonlinear even for linear elastic materials as well as the static equilibrium constraint. Therefore, the adjoint method⁷² is often applied to avoid solving the nonlinear Karush–Kuhn–Tucker (KKT) system as in equality constrained optimization.⁷³ It takes \mathbf{u} as a function of \mathbf{x} and cancels out $\frac{\partial \mathbf{u}}{\partial \mathbf{x}}$ by considering the searching process to be conducted only on the force equilibrium constraint manifold. Given an intermediate state ρ , the PDE constraint has to hold by solving the displacement field \mathbf{u} at static equilibrium for each iteration. For linearly elastic materials, finding the static equilibrium results in solving a linear system of equations, which is generally considered the topology optimization's bottleneck. Therefore, obtaining intricate structural features by increasing resolution demands extra computational powers or carefully designed implementations.^{1,2} It becomes even more challenging for nonlinear hyperelastic materials because a nonlinear system of equations needs to be solved at each optimization iteration, leading to numerical instabilities.

2.2 | Lagrangian–Eulerian multidensity topology optimization

A hybrid Lagrangian–Eulerian approach is proposed to establish a versatile topology optimization framework that can accommodate different elastic models to address the aforementioned challenges. In particular, the elastic potential as the compliance objective is optimized for both linear and highly nonlinear (e.g., neo-Hookean) elastic materials. A set of carrier particles is adopted to represent the material distribution and evolution. Each particle is a moving material sample carrying the information of position \mathbf{x}^c , density ρ^c , and supporting radius. This modifies the general formulation in Equation (1) from a pure Eulerian representation, which directly optimizes the density field ρ , to a hybrid Lagrangian–Eulerian form, which jointly optimizes \mathbf{x}^c and ρ^c that define the material distribution $\rho(\mathbf{x}^c, \rho^c)$ over the design domain:

$$\min_{\mathbf{x}^c, \rho^c} c(\rho(\mathbf{x}^c, \rho^c), \mathbf{u}) = e(\rho(\mathbf{x}^c, \rho^c), \mathbf{u}) \quad \text{s.t.} \quad \begin{cases} \frac{\partial e}{\partial \mathbf{u}}(\rho(\mathbf{x}^c, \rho^c), \mathbf{u}) = \mathbf{f} \\ \mathbf{D}\mathbf{u} = \mathbf{0} \\ V(\rho(\mathbf{x}^c, \rho^c)) \leq \hat{V}. \end{cases} \quad (6)$$

Using MPM as the static equilibrium solver, the design domain is discretized with an Eulerian background grid and a set of uniformly sampled quadrature points in each grid cell where every quadrature has its independent density value. These quadrature points jointly form the scalar field ρ . In this way, a subcell resolution is naturally resolved through multiple quadratures per cell. The relation between carrier particles (\mathbf{x}^c, ρ^c) and quadrature points (ρ) is further constructed using SPH kernel and a sharp density mapping function. Adopting the SPH kernel has the equivalent effect as the gradient filter⁴ that prevents the checkerboard pattern. However, since the SPH kernel is directly incorporated in the objective, it avoids performing any extra smoothing on the gradient, keeping the search direction and the objective consistent.

To efficiently solve the static equilibrium, it is straightforward to achieve a narrow-band sparse simulation² using MPM by filtering out low-density quadratures. This is essentially equivalent to how zero-mass grid nodes are filtered out in MPM-based dynamic simulations. This mechanism is also adopted to eliminate QR patterns by maintaining a single main connected component to filter out isolated material blocks. The narrow-band filter threshold's increment replaces the Heaviside projection in traditional density-based topology optimization algorithm for producing binarized designs.

Using moving asymptotes (MMA)⁷⁴ as the optimizer, the optimization pipeline can be summarized as the follows; also see an illustration in Figure 2.

0. **Initialize:** Collocate carrier particles on the uniformly sampled MPM quadrature points and initialize carrier particle density ρ^c with the target volume prescription such that the volume constraint is satisfied; see Section 3.1.
1. **Transfer information from carrier particles to quadrature points (C2P):** Transfer density from carrier particles to quadrature points ($\rho(\mathbf{x}^c, \rho^c)$) with a spherical kernel and a sharp density mapping function; see Section 3.1.
2. **MPM Static Solve;** see Section 3.3.
 - 2.1. **Transfer information from quadrature points to grid (P2G):** Extract the main connected component using the narrow-band filter; see Section 3.4. Transfer density from quadrature points in the main connected component to grid nodes and construct the MPM system matrix $\frac{\partial^2 e}{\partial \mathbf{u}^2}$ on the grid. Untouched grids are dropped out of degrees of freedom.
 - 2.2. **Solve force equilibrium:** Solve $\frac{\partial e}{\partial \mathbf{u}} = \mathbf{f}$ for the displacement field \mathbf{u} on the MPM grid subject to Dirichlet boundary conditions $\mathbf{D}\mathbf{u} = \mathbf{0}$. Here, only solving a single linear system is required for material with a linear elastic

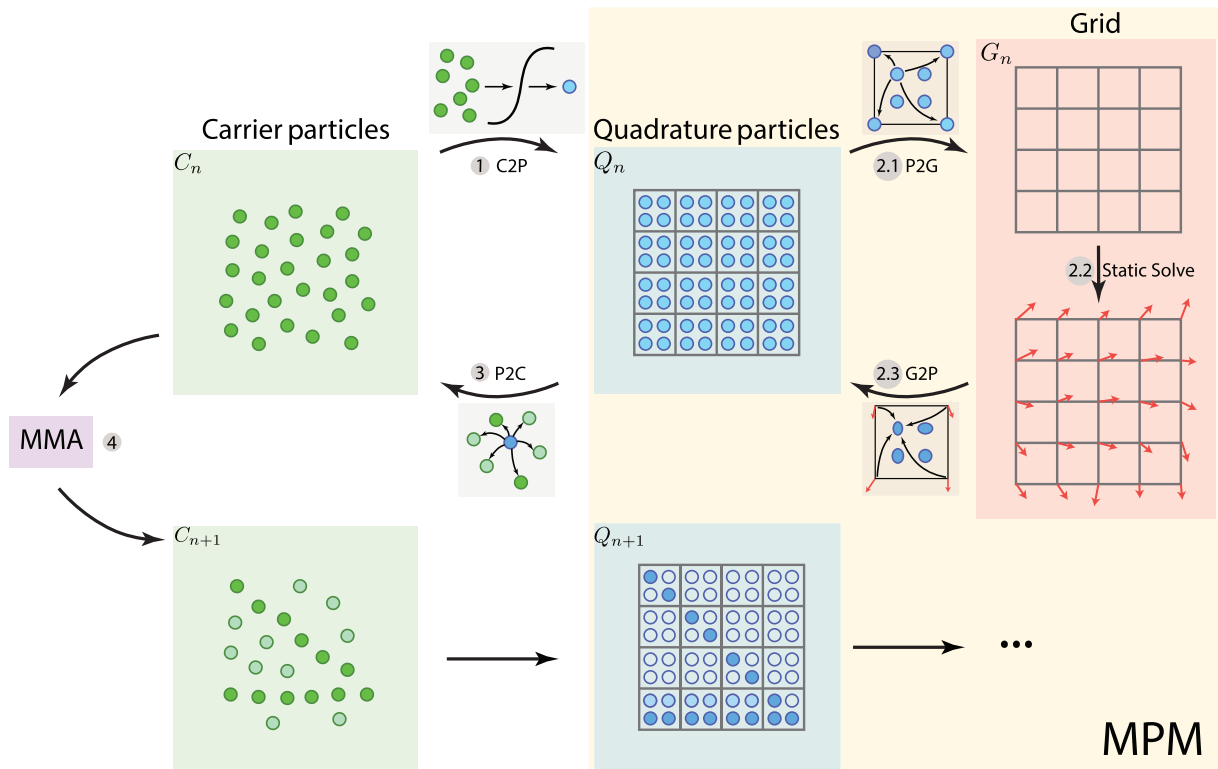


FIGURE 2 Hybrid Lagrangian–Eulerian method pipeline with an material point method solver

material (see Section 3.2.1). On the other hand, the projected Newton method with line search that guarantees stability and convergence is applied for nonlinearly elastic materials (see Section 3.3.2).

- 2.3. **Update quadrature deformation gradient (G2P):** Update the deformation gradient F_q of quadrature points with the solved nodal displacement field \mathbf{u} .
3. **Compute compliance and the derivatives (P2C):** Evaluate compliance objective $e(\mathbf{p}, \mathbf{u})$ (Equation (25)), compliance derivative $de/d\{\mathbf{x}^c, \mathbf{p}^c\}$ (Equation (19)), volume V (Equation (15)), and volume derivative $dV/d\{\mathbf{x}^c, \mathbf{p}^c\}$ (Equation (16)) for optimization search; see Section 3.2.
4. **Update carrier particle data:** Update $\mathbf{x}^c, \mathbf{p}^c$ using MMA and evaluate convergence criteria; see Section 4.1. If not converged, go to Step 1 and repeat.
5. **Graph-based connectivity correction:** Correct quadrature connectivity according to grid connectivity where the static equilibrium is evaluated; see Section 3.4.

3 | HYBRID LAGRANGIAN-EULERIAN MULTIDENSITY METHOD

3.1 | Material distribution representation

Introducing Lagrangian degrees of freedom by optimizing quadrature positions together with quadrature densities is a straightforward choice. However, arbitrary movements of quadrature may cause large numerical errors, which can even lead to degeneracies like quadrature clustering and isolation. Thus, another set of moving carrier particles is introduced as the design variables to re-parameterize the density field space and, at the same time, to avoid moving quadrature points. Carrier particles are defined in the entire design domain with Lagrangian variables $\xi = (\mathbf{x}^c, \mathbf{p}^c)$ consists of both position and density. The final material distribution and the volume constraint are still discretized on quadrature points, where their densities are computed according to the surrounding carrier particles. In the proposed method, the carrier particles are crucial in emerging intricate geometry structures (see Figure 3).

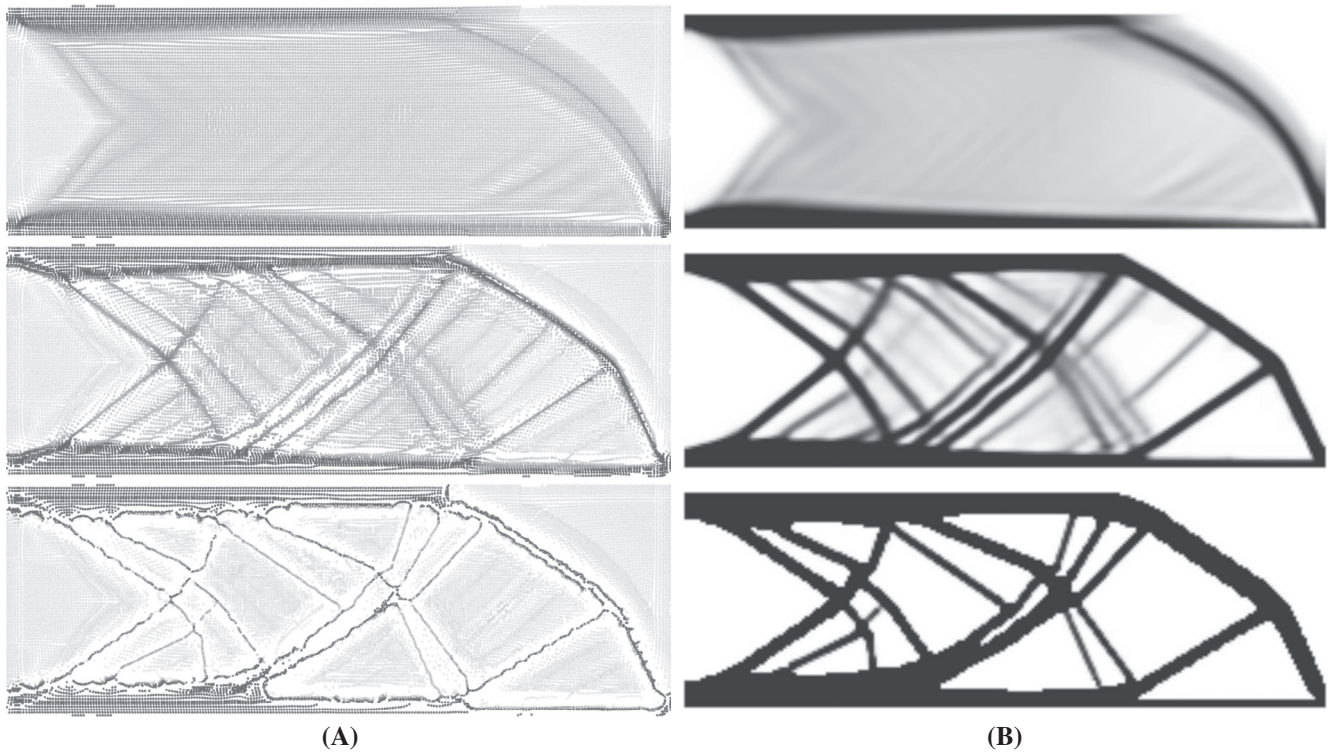


FIGURE 3 Optimization evolution on carrier and quadrature points. (A) The position and density changes of carrier particles. (B) The density changes on quadrature points

The density of each quadrature point q is defined as the weighted sum of its neighboring carrier particles $\{\alpha\}$ using an SPH kernel:

$$\tilde{\rho}_q = \sum_{\alpha} \int_{\Omega} \rho_{\alpha}^c W\left(\frac{|\mathbf{x}_{\alpha}^c - \mathbf{X}|}{h}\right) d\mathbf{X} \approx \sum_{\alpha} \rho_{\alpha}^c W\left(\frac{|\mathbf{x}_{\alpha}^c - \mathbf{x}_q|}{h}\right) V_{\alpha}, \quad (7)$$

where $W(R)$ is a kernel function, h is the kernel size, and V_{α} is the volume of each quadrature, which equals to $(\frac{\Delta x}{2})^d$ when 2^d quadratures are sampled in each cell. In this paper, the kernel function with cubic spline is applied:

$$W(R) = \sigma \begin{cases} 1 - \frac{3}{2}R^2 + \frac{3}{4}R^3, & 0 < R < 1 \\ \frac{1}{4}(2 - R)^3, & 1 < R < 2 \\ 0, & \text{otherwise} \end{cases} \quad (8)$$

where σ is a constant of $\frac{10}{7\pi h^2}$ in two dimensional (2D) and $\frac{1}{\pi h^3}$ in three dimensional (3D).

The derivative of $\tilde{\rho}_q$ w.r.t. the design variables is given by

$$\frac{\partial \tilde{\rho}_q}{\partial \mathbf{x}_{\alpha}^c} = \rho_{\alpha}^c \frac{\partial W}{\partial \mathbf{x}_{\alpha}^c} V_{\alpha}, \quad (9)$$

and

$$\frac{\partial \tilde{\rho}_q}{\partial \rho_{\alpha}^c} = W\left(\frac{|\mathbf{x}_{\alpha}^c - \mathbf{x}_q|}{h}\right) V_{\alpha}. \quad (10)$$

To prevent the densities of quadrature particles from exceeding one, a smooth clamping function is further added on top of $\tilde{\rho}_q$ (see Figure 4):

$$\hat{\rho}(\tilde{\rho}) = \begin{cases} \tilde{\rho}, & 0 \leq \tilde{\rho} < 1 - \epsilon \\ \frac{(\tilde{\rho} + \epsilon - 1)^2}{4\epsilon} + \tilde{\rho}, & 1 - \epsilon \leq \tilde{\rho} < 1 + \epsilon \\ 1, & \tilde{\rho} \geq 1 + \epsilon \end{cases} \quad (11)$$

and its derivative is

$$\frac{\partial \hat{\rho}}{\partial \tilde{\rho}} = \begin{cases} 1, & 0 \leq \tilde{\rho} < 1 - \epsilon \\ \frac{(\tilde{\rho} + \epsilon - 1)}{2\epsilon} + 1, & 1 - \epsilon \leq \tilde{\rho} < 1 + \epsilon \\ 0, & \tilde{\rho} \geq 1 + \epsilon \end{cases} \quad (12)$$

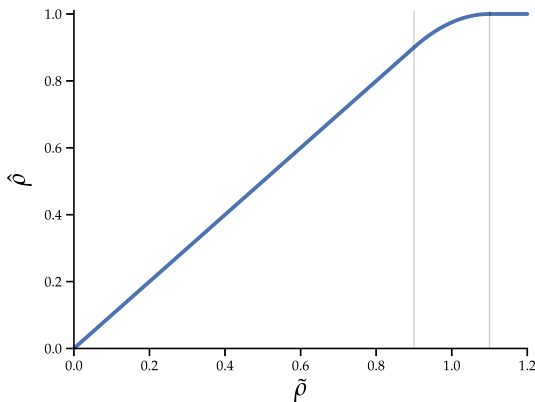


FIGURE 4 Density mapping function

If $\tilde{\rho}$ is greater than $1 + \epsilon$, the output will be one, and the derivative will be zero. Consequently, through chain-rule, the gradients w.r.t. the design variables vanish, which successfully prevent aggregation of particles. Otherwise, stiffer material than allowed can be formed by gathering particles, leading to nonphysical material.

Finally, the density of each quadrature q is given by,

$$\rho_q = \hat{\rho}(\tilde{\rho}), \quad (13)$$

and its derivative is

$$\frac{d\rho_q}{d\xi} = \frac{d\hat{\rho}_q}{d\tilde{\rho}_q} \frac{d\tilde{\rho}_q}{d\xi}. \quad (14)$$

The volume of the structure is given by

$$V(\xi) = \sum_q \rho_q, \quad (15)$$

where q indices all quadrature points, and its derivative is

$$\frac{dV}{d\xi} = \sum_q \frac{\partial \rho_q}{\partial \tilde{\rho}} \frac{\partial \tilde{\rho}}{\partial \xi}, \quad (16)$$

The densities of carrier particles are initialized to a uniform scale such that the density of each quadrature is equal to the prescribed volume fraction (the prescribed volume divided by the domain volume). Since the clamping function is only nonlinear after $1 - \epsilon$, by the partition-of-unity property of SPH kernel, the initial volume is very close to the target volume, where the error comes from the approximation in Equation (7). Also note that since the volume constraints are defined on quadrature volumes and the output structure is also represented by quadratures with nonzero density values, there is no need to consider the mass/volume conservation during carrier-quadrature transfers.

3.2 | Design sensitivity analysis

To compute the derivatives of the compliance objective e w.r.t. design variables ξ required for the topology optimization, the searching process of finding the adjoint variables is constrained to be solely on the force equilibrium manifold.

$\frac{de}{d\xi}$ can be expressed via applying the chain rule as

$$\frac{de}{d\xi} = \left[\frac{d\boldsymbol{\rho}}{d\xi} \right]^T \left(\frac{\partial e}{\partial \boldsymbol{\rho}} + \left[\frac{d\mathbf{u}}{d\boldsymbol{\rho}} \right]^T \frac{\partial e}{\partial \mathbf{u}} \right). \quad (17)$$

Here $\frac{d\mathbf{u}}{d\boldsymbol{\rho}}$ is difficult to compute as \mathbf{u} and $\boldsymbol{\rho}$ are related by the force equilibrium equation; even the evaluation of \mathbf{u} from $\boldsymbol{\rho}$ requires solving a system of equations. However, if the searching process is constrained to be only on the constraint manifold defined by the force equilibrium equation, differentiating $\frac{\partial e}{\partial \mathbf{u}} = \mathbf{f}$ w.r.t. $\boldsymbol{\rho}$ provides

$$\frac{\partial^2 e}{\partial \boldsymbol{\rho} \partial \mathbf{u}} + \left[\frac{d\mathbf{u}}{d\boldsymbol{\rho}} \right]^T \frac{\partial^2 e}{\partial \mathbf{u}^2} = 0, \quad (18)$$

then Equation (17) can be simplified by combining with Equation (18) into

$$\frac{de}{d\xi} = \left[\frac{d\boldsymbol{\rho}}{d\xi} \right]^T \left(\frac{\partial e}{\partial \boldsymbol{\rho}} - \frac{\partial^2 e}{\partial \boldsymbol{\rho} \partial \mathbf{u}} \left[\frac{\partial^2 e}{\partial \mathbf{u}^2} \right]^{-1} \mathbf{f} \right), \quad (19)$$

which is the final derivative, where the compliance e can be defined by either linear or nonlinear elasticity.

3.2.1 | Simplification under linear elasticity

The computation of derivative $\frac{de}{d\rho}$ requires solving a linear system. However, when linear elasticity is applied, it can be simplified to the form widely used in linear topology optimization.⁴

Specifically, when linear elasticity is utilized, the matrix $\frac{\partial^2 e}{\partial \mathbf{u}^2}$ is constant, so the internal elasticity force is linear w.r.t \mathbf{u} , and the potential e is quadratic w.r.t. \mathbf{u} . Namely,

$$\begin{aligned} e &= \frac{1}{2} \mathbf{u}^T \mathbf{K} \mathbf{u}, \quad \mathbf{f} = \frac{\partial e}{\partial \mathbf{u}} = \mathbf{K} \mathbf{u}, \quad \frac{\partial^2 e}{\partial \mathbf{u} \partial \mathbf{u}} = \mathbf{K}, \\ \frac{\partial e}{\partial \rho} &= \frac{1}{2} \mathbf{u}^T \frac{\partial \mathbf{K}}{\partial \rho} \mathbf{u}, \quad \frac{\partial^2 e}{\partial \rho \partial \mathbf{u}} = \mathbf{u}^T \frac{\partial \mathbf{K}}{\partial \rho}, \end{aligned} \quad (20)$$

where \mathbf{K} is the stiffness matrix depending on densities ρ . Substituting these equations into Equation (19), it follows that

$$\frac{de}{d\rho} = \frac{1}{2} \mathbf{u}^T \frac{\partial \mathbf{K}}{\partial \rho} \mathbf{u} - \mathbf{u}^T \frac{\partial \mathbf{K}}{\partial \rho} \mathbf{K}^{-1} \mathbf{f} = -\frac{1}{2} \mathbf{u}^T \frac{\partial \mathbf{K}}{\partial \rho} \mathbf{u}, \quad (21)$$

which is exactly the same form derived in traditional linear topology optimization via the adjoint method. For arbitrary design variables ξ , applying the chain-rule, the derivative becomes

$$\frac{de}{d\xi} = -\frac{1}{2} \left[\frac{d\rho}{d\xi} \right]^T \left[\mathbf{u}^T \frac{\partial \mathbf{K}}{\partial \rho} \mathbf{u} \right]. \quad (22)$$

3.3 | MPM discretization for multidensity topology optimization

In MPM, the design domain Ω is discretized with a set of material particles, or quadratures to approximate the integrals in Equation (1), which are computed as the weighted sum over all the quadratures:

$$e(\rho, \mathbf{u}) = \int_{\Omega} \Psi(\mathbf{F}) dX \approx \sum_q \Psi(\mathbf{F}_q) V_q. \quad (23)$$

$$V(\rho) = \int_{\Omega} \rho(\mathbf{X}) dX \approx \sum_q \rho_q V_q. \quad (24)$$

where q indices all quadrature points, and each quadrature q has its own density ρ_q , Young's modulus E_q , deformation gradient \mathbf{F}_q , elastic energy density function Ψ_q , and volume V_q . To get a sufficiently aligned density field, 2^d quadrature points in each cell are sampled on a regular lattice structure as illustrated in Figure 2. With MPM discretization, multiple densities per cell can be handled in a straightforward manner.

Similarly to SIMP, Young's modulus is scaled by the powered density of the particle: $E_q = \rho_q^p E_0$, where E_0 is the material's Young's modulus, so that the stiffness of the material is continuously varying over the domain according to its distribution. Since Ψ is linear w.r.t. Young's modulus, the compliance can be rewritten as

$$e(\rho, \mathbf{u}) = \sum_q \rho_q^p \Psi_0(\mathbf{F}_q) V_q, \quad (25)$$

where Ψ_0 is the energy density function with Young's modulus E_0 .

3.3.1 | Static equilibrium

While MPM is commonly used for dynamic time-stepping, a static problem formulation based only on MPM spatial discretization similar to the total Lagrangian formulation⁷⁵ is needed for topology optimization. In such a static setting, there is no inertia effect or time-variant variables, meaning that only the elasticity and external force terms are kept:

$$-\frac{\partial e}{\partial \mathbf{u}}(\rho, \mathbf{u}) + \mathbf{f} = \mathbf{0}, \quad (26)$$

where \mathbf{f} is the external body force load (Neumann boundary condition) defined on the grid nodes. Dirichlet boundary conditions can be defined as

$$\mathbf{D}\mathbf{u} = \mathbf{0}, \quad (27)$$

where \mathbf{D} is the selection matrix that extracts the Dirichlet grid nodes. From a variational point of view, this is equivalent to solving the following optimization problem

$$\min_{\mathbf{u}} e(\boldsymbol{\rho}, \mathbf{u}) - \mathbf{u}^T \mathbf{f} \quad \text{s.t.} \quad \mathbf{D}\mathbf{u} = \mathbf{0}. \quad (28)$$

In MPM, quadratures are embedded in the background Eulerian grid with a B-spline kernel, meaning that the nodal displacement \mathbf{u} is, in fact, defined on the uniform grid nodes. Since in LETO elastostatic problems are solved without material particle (quadrature points) advection, there will be no cell crossing errors or ringing instabilities for MPM even if linear kernel is used for simplicity:

$$N(x) = \begin{cases} 1 - |x|, & 0 \leq x < 1 \\ 0, & 1 \leq x. \end{cases} \quad (29)$$

Here the weight ω_{iq} between grid node location \mathbf{x}_i and quadrature location \mathbf{x}_q is defined by taking the Cartesian product in all dimensions. For example, in 3D,

$$\omega_{iq}(x_q) = N\left(\frac{1}{h}(x_{q,1} - x_{i,1})\right) N\left(\frac{1}{h}(x_{q,2} - x_{i,2})\right) N\left(\frac{1}{h}(x_{q,3} - x_{i,3})\right); \quad (30)$$

and in 2D,

$$\omega_{iq}(x_q) = N\left(\frac{1}{h}(x_{q,1} - x_{i,1})\right) N\left(\frac{1}{h}(x_{q,2} - x_{i,2})\right). \quad (31)$$

The deformation gradient F_q on quadrature q is then related to the surrounding grid nodes i as

$$\mathbf{F}_q = \mathbf{I} + \sum_i \mathbf{u}_i \nabla \omega_{iq}^T, \quad (32)$$

which also leads to the elasticity force definition

$$-\frac{\partial \mathbf{e}}{\partial \mathbf{u}} = -\sum_q \rho_q^p V_q^0 \frac{\partial \Psi_0(\mathbf{F}_q)}{\partial \mathbf{F}_q} \nabla \omega_{iq}, \quad (33)$$

and the elasticity Hessian (in index notation)

$$\frac{\partial^2 e}{\partial u_{i,\alpha} \partial u_{j,\beta}} = \sum_q \rho_q^p V_q^0 (\nabla \omega_{iq})_\delta \frac{\partial^2 \Psi_0(F_q)}{\partial F_{q,\alpha\delta} \partial F_{q,\beta\omega}} (\nabla \omega_{jq})_\omega, \quad (34)$$

where $1 \leq \alpha, \beta, \delta, \omega \leq d$ and d is the spatial dimension. $F_{q,\alpha\beta}$ is (α, β) th element of the deformation gradient F_q .

Compared with the MPM formulation for dynamic problems, the static formulation can be seen as only solving for a single “time step,” and the deformation gradient at previous time step, \mathbf{F}_q^n , is just the initial undeformed deformation gradient $\mathbf{F}_q^n = \mathbf{F}_q^0 = \mathbf{I}$.

3.3.2 | Static solve with projected Newton

To solve the equilibrium equation more robustly, the variational form (Equation (28)) is minimized with the projected Newton’s method⁶⁸ as outlined in Algorithm 1. Dirichlet boundary conditions are handled by modifying the

corresponding entries in the matrix and the right-hand-side to keep the problem unconstrained, which is equivalent to eliminating the Lagrange multipliers in the KKT system with linear equality constraints. The stopping criteria is chosen to be $\|\Delta \mathbf{u}\|_\infty < \tau = 0.1\Delta \mathbf{x}$. Note that when a linear constitutive model is used, the system is quadratic, so only one iteration is needed.

Algorithm 1. Projected Newton for solving static equilibrium

```

1: procedure PROJECTEDNEWTON( $\rho^j, \mathbf{f}, \mathbf{D}, \tau, \mathbf{u}$ )
2:    $\Delta \mathbf{u} = \mathbf{0}, \mathbf{u}^0 = \mathbf{0}, i = 0$  // initialize
3:   do
4:      $\mathbf{P} \leftarrow \text{projectSPD}(\frac{\partial^2 e}{\partial \mathbf{u}^2})$  // project each local Hessian stencil to SPD68
5:      $\Delta \mathbf{u} \leftarrow \mathbf{P}^{-1}(\mathbf{f} - \frac{\partial e}{\partial \mathbf{u}})$ 
6:      $\alpha \leftarrow \text{LineSearch}(\mathbf{u}^i, \Delta \mathbf{u})$  // Back-tracking line-search
7:      $\mathbf{u}^{i+1} \leftarrow \mathbf{u}^i + \alpha \Delta \mathbf{u}$ 
8:      $i \leftarrow i + 1$ 
9:   while  $\|\Delta \mathbf{u}\|_\infty \geq \tau$ 
10:   $\mathbf{u} \leftarrow \mathbf{u}^i$ 
11: end procedure

```

3.3.3 | Inversion-free line search

Since in each projected Newton iteration, the Hessian has been projected to symmetric positive definite, the search direction $\Delta \mathbf{u}$ is guaranteed to be a descent direction. Therefore, back-tracking line search can ensure $E(\mathbf{u}^{i+1}) < E(\mathbf{u}^i)$ after each \mathbf{u} update, which effectively stabilizes the iterations and improves convergence.

However, for the noninvertible elasticity energy (neo-Hookean), projected Newton does not necessarily ensure no deformation gradient inversion along search direction $\Delta \mathbf{u}$. Hence, following Smith and Schaefer,⁷⁶ to further prevent inversion of each \mathbf{F}_q , a large feasible step size before each line search is solved by finding the minimum of the smallest positive roots of a family of equations

$$\{\det(\mathbf{F}_q(\mathbf{u}^i + \beta_q \Delta \mathbf{u})) = \epsilon_q\}. \quad (35)$$

The line search step size then starts from $\min_q \beta_q$. Here, $\epsilon_q = 0.1 \det(\mathbf{F}_q(\mathbf{u}^i))$ is used to avoid numerical rounding errors, which is more robust than solving with $\epsilon_q = 0$.

3.4 | Narrow-band filter and connectivity correction

Multidensity topology optimization methods suffer from a common artifact known as QR patterns. Unlike the traditional checkerboard problem, QR patterns happen on a subcell level, which corresponds to the quadrature here. When QR patterns appear, there are many subcell level isolation of the solid components, which are still viewed as connected from the perspective of the background grid where forces and displacements are discretized. This kind of inconsistency prevents simulation from accurately predicting a structure's compliance, which can lead to results with large compliance when tested in practice or simulated on a grid with higher resolution. Based on this observation, this paper proposes a narrow-band filter to keep only one major connected component during the optimization and then apply a connectivity correction step to correct the final topology further.

Given a threshold η , a graph is built at each optimization iteration before the static solve, with its vertices being those quadrature points having a density greater than η . Quadrature pairs are identified to be adjacent only if their Manhattan distance is 1 (adjacent along one of the coordinate axes). By performing a breadth-first search on this graph, the connected component Θ with the most quadrature points are then extracted. Only the grid nodes within the kernel range of active quadrature points are kept as Degrees of Freedom (DOFs) in the MPM static solve step. An illustration is shown in Figure 5.

The narrowband filter θ employed is introduced as:

$$\theta(\rho_q) = \begin{cases} 0, & q \in \Theta \\ 1, & q \notin \Theta, \end{cases} \quad (36)$$

with which the topology optimization becomes:

$$\min_{\xi, \mathbf{u}} e(\boldsymbol{\rho}, \mathbf{u}) = \sum_q \theta(\rho_q) \rho_q^p \Psi_0(\mathbf{F}_q) V_q, \quad \text{s.t.} \quad \begin{cases} \frac{\partial e}{\partial \mathbf{u}}(\boldsymbol{\rho}, \mathbf{u}) = \mathbf{f} \\ \mathbf{D}\mathbf{u} = \mathbf{0} \\ V(\boldsymbol{\rho}) \leq \hat{V}. \end{cases} \quad (37)$$

To handle the nonsmoothness of θ , an alternating optimization style strategy is performed that computes θ between each MMA optimization iteration where θ is then treated as constant. Theoretically, this strategy can lead to different local optimum compared to a fully coupled search, but it has been shown to be effective in our experiments. During the optimization, the narrow-band filter can also accelerate the pruning of redundant branches, for example, a fiber with only one end connected to the major component, which can increase the compliance.

Given that the narrow-band filter can remove all quadrature points with a density below η , a new binary design enforcement mechanism is proposed. A low threshold of the narrow-band filter is chosen initially for a coarse but more global result and is further increased per iteration towards a value very close to 1 (Figure 6). This mechanism provides better optimization stability by enforcing binary design without any nonlinear projections, for example, a Heaviside function.

However, QR patterns may still exist when the two parts of the major component's boundaries are spatially close. Figure 7 lists some illustrated examples. Here the filled and unfilled circles are used to discriminate solid and void materials. It can be seen that despite a notable disconnection of quadrature points, when evaluating the static force equilibrium, these are still considered connected since they can belong to the same cell (the left example) or adjacent cells (the right example). However, when evaluating the resulting design, a double-refined grid where each quadrature corresponds to a different cell, the corresponding cells of these separated quadratures will only share one node or are completely disconnected. To detect and remove these QR patterns, a connectivity correction step is further introduced: for any pair of quadratures belonging to the same cell or two different cells sharing at least one node, if the difference between their

FIGURE 5 An illustration of the narrowband filter mechanism. An active area is first extracted by the graph connectivity. Active DOFs are then indicated by whether they belongs to cells with active quadratures. Only active DOFs are kept for the static solve to reduce the computational cost

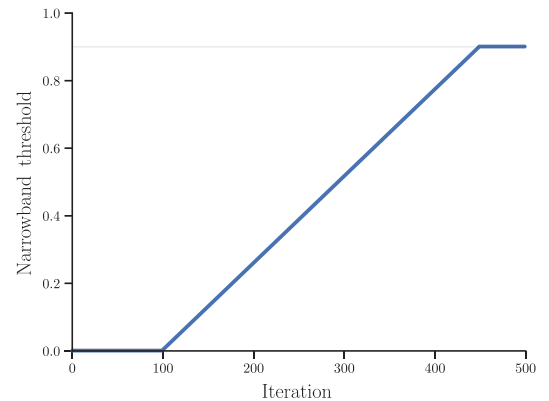
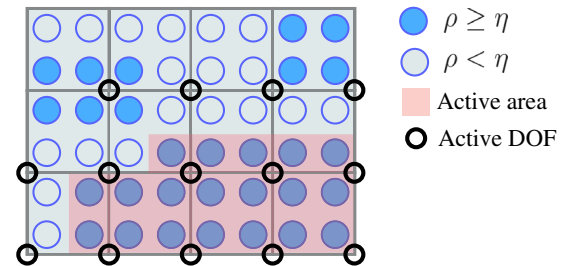


FIGURE 6 Evolution of narrowband threshold

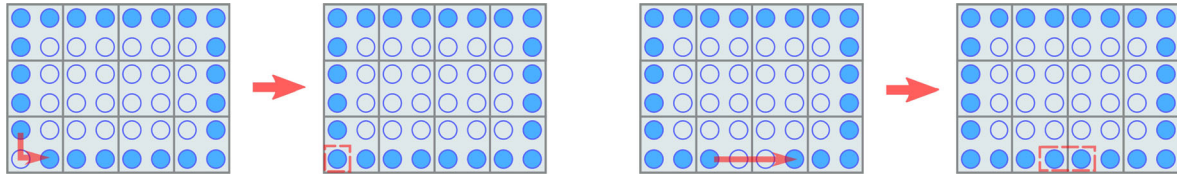


FIGURE 7 Illustrated examples of emerging QR patterns and connectivity correction procedures

distance on the graph (the length of the shortest path) and their spatial L_1 distance is larger than a threshold, a shortest Manhattan path will be created between them with the densities along the path all set to 1. Note that the occurrence of such corrections is rare.

4 | NUMERICAL EXAMPLES

4.1 | Optimizing structures with MMA

The method of moving asymptotes (MMA)⁷⁴ is used to solve the optimization problem, which jointly optimizes the positions and densities of carrier particles. This optimizer is designed for general structural optimization problems with inequality constraints and box constraints. The algorithm approximates the original problem with a series of separable convex optimizations. At each iteration, it sets up two asymptotes for each variable to constrain the searching interval. These asymptotes will be updated according to each suboptimum. In our implementation, we adopt an open-source C++ version of MMA.*

To obtain high-quality results from MMA, careful parameter tuning is necessary, and different examples might have different sets of optimal MMA parameters. There are three parameters to tune: *asyinit*, *asyincr*, and *asydecr*. In this paper, these parameters are set to be 0.02, 1.05, and 0.65, respectively, as in the original MMC method. The parameters are used throughout all the numerical examples. To further stabilize and accelerate the optimization in a consistent way, the following regularizations are additionally applied within MMA :

1. The step length of each variable is controlled by modifying its box constraint at each iteration. The change of carrier density is controlled to be below 0.5, and the change of carrier position at each dimension is controlled to be below 2 times the background grid spacing. This step size control can stabilize optimization.
2. Following the MMC method, the gradient of objective and the volume constraint are scaled such that their L^∞ -norms are both 1. In addition, the objective and the volume constraint are scaled accordingly to make sure the scaled gradients are consistent. The scaling accelerates the optimization significantly.

4.2 | Linear topology optimization

In this section, the proposed method is compared with SIMP with Heaviside projection⁷⁷ on linear elasticity examples. The filter radius of SIMP is 1.5 for all examples. Under the same simulation resolution, LETO obtains more detailed geometry structures and delivers comparable or even lower compliance at a similar convergence speed (see Figure 8). For fair comparisons, LETO and SIMP's final results are compared on a double refined grid using FEM, where individual quadrature of LETO corresponds to a cell on the refined grid. Each cell of SIMP is mapped to a 2×2 (in 2D) or $2 \times 2 \times 2$ (in 3D) cell block with the same density. As varying volumes can easily lead to compliance changes, to further ensure fairness, the final volume constraint of LETO is controlled to be slightly lower than the corresponding volume in the SIMP method. For each of the following experiments, SIMP is first tested with the target volume. The volume constraint of LETO is then set to be less than the volume of the binarized SIMP's result. Since LETO treats volume constraints as inequalities through MMA, it usually ends up with an even slightly smaller volume. The binarization threshold of SIMP is set to be 0.5. Since LETO can guarantee there exists no density values between 0 and 0.9, the binarization threshold of LETO is chosen

*<https://github.com/jdumas/mma>

to be 0.9. To demonstrate that QR-patterns do not appear in the proposed method's final results, compliance values are evaluated at both the resolution used in optimization and with double-resolution. A collection of resulting compliance value and volume percentage of five experiments is shown in Table 1. The average computational costs per iteration are also shown. Since MMA used in LETO is usually slower than OC used in SIMP, it is expected that LETO is slower than SIMP. However, the narrowband filter can prune inactive DOFs, which can reduce the computational cost a lot after the structure becomes sufficiently binarized (especially in 3D).

4.2.1 | 2D beam with a concentrated load

In this example, a standard 2D beam benchmark problem is tested; see Figure 9. The rectangular design domain is 1 m in width and 3 m in length, discretized by a 300×100 grid with a spacing of 0.01 m. A 0.1 N downward force is concentrated at

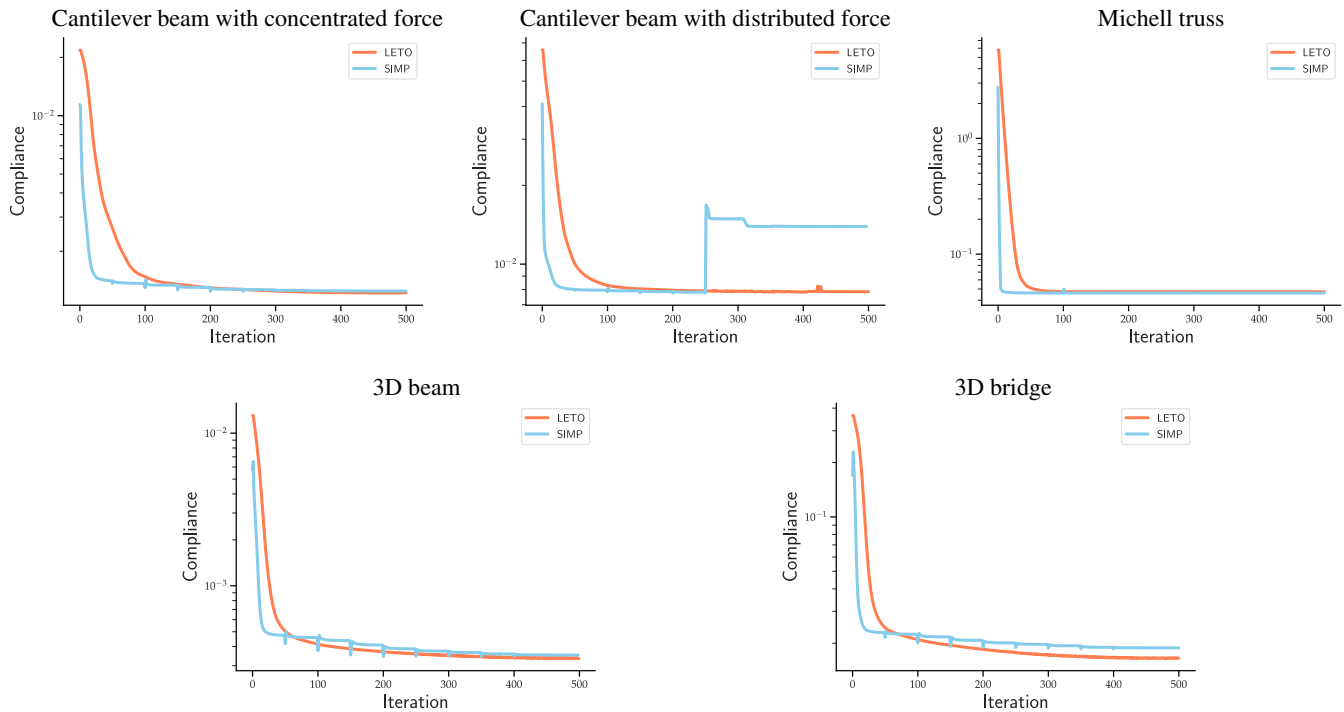


FIGURE 8 Convergence plots for linear elasticity experiments. It can be seen here in the five experiments conducted, Lagrangian–Eulerian topology optimization (LETO) achieves comparable structural compliance value and convergence speed. Notably, under distributed force condition, LETO delivers better stability

TABLE 1 Compliance value and volume percentage for linear elastic experiments. The compliance value of results from the proposed method under optimization grid resolution, under double-refined grid resolution and Solid Isotropic Material with Penalization Method (SIMP) method under double-refined grid resolution is shown in this table

Experiment	LETO				SIMP ($r = 1.5$)		
	Compliance	Compliance (refined grid)	Volume	Ave. cost (per iter.)	Compliance (refined grid)	Volume	Ave. cost (per iter.)
Concentrated-load beam	1.218×10^{-3}	1.243×10^{-3}	29.9%	0.405 s	1.264×10^{-3}	30.1%	0.387 s
Michell truss	4.736×10^{-2}	5.054×10^{-2}	20.1%	0.544 s	5.055×10^{-2}	20.2%	0.355 s
Distributed-load beam	7.845×10^{-3}	8.386×10^{-3}	39.7%	0.867 s	1.658×10^{-2}	40.0%	0.408 s
3D beam	3.323×10^{-4}	3.334×10^{-4}	19.6%	3.753 s	3.527×10^{-4}	20.0%	6.110 s
3D bridge	1.653×10^{-2}	1.643×10^{-2}	19.4%	6.893 s	1.892×10^{-2}	20.0%	16.816 s

the bottom-right grid node (denoted by the red arrow) and the leftmost grid nodes are fixed. The target volume constraint is 30%. The optimal material distribution obtained from LETO has rich branching fibers. Even the thick fibers on the boundary of SIMP's result splits into several thin fibers in LETO. The compliance of LETO's result evaluated at optimization resolution and double resolution, and SIMP's result evaluated at double resolution are 1.218×10^{-3} , 1.243×10^{-3} , and 1.264×10^{-3} respectively. The final volume reached by LETO and SIMP are 29.9% and 30.1%.

4.2.2 | Michell Truss

The second example under consideration is Michell truss; see Figure 10. A $2 \text{ m} \times 1.6 \text{ m}$ rectangle is used as the design domain. The grid resolution is 200×160 with a spacing of 0.01 m . A concentrated downward force of 1 N is applied to the middle node of the leftmost column of the grid. The middle region of the right-most grid is set to be fixed. The target volume is 20%. The compliance of SIMP evaluated at double resolution, LETO evaluated at optimization resolution, and double resolution are 5.055×10^{-2} , 4.736×10^{-2} , 5.054×10^{-2} , respectively. Although LETO's result has almost the same compliance as SIMP, it resembles more to the analytical solution⁷⁸ as can be seen from the resulting fiber direction. The final volume reached by SIMP and LETO is 20.2% and 20.1%.

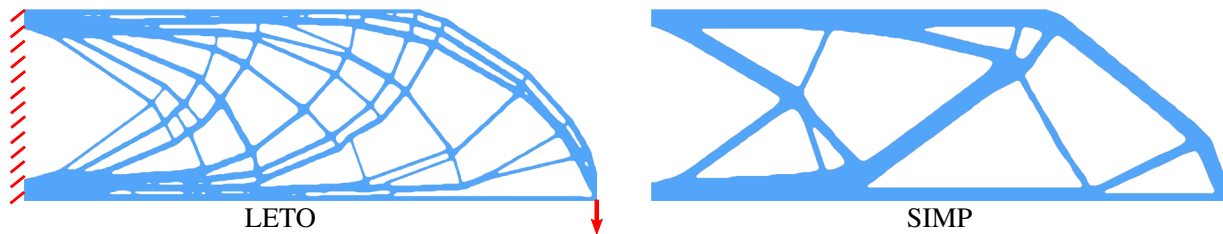


FIGURE 9 Two-dimensional beam with a concentrated load. The comparison between LETO and SIMP on this standard 2D beam example where left most grid nodes are fixed, and a concentrated load is applied at the bottom-right corner. The compliance value evaluated at double-refined grid resolution for LETO and SIMP are 1.243×10^{-3} and 1.264×10^{-3} , respectively.

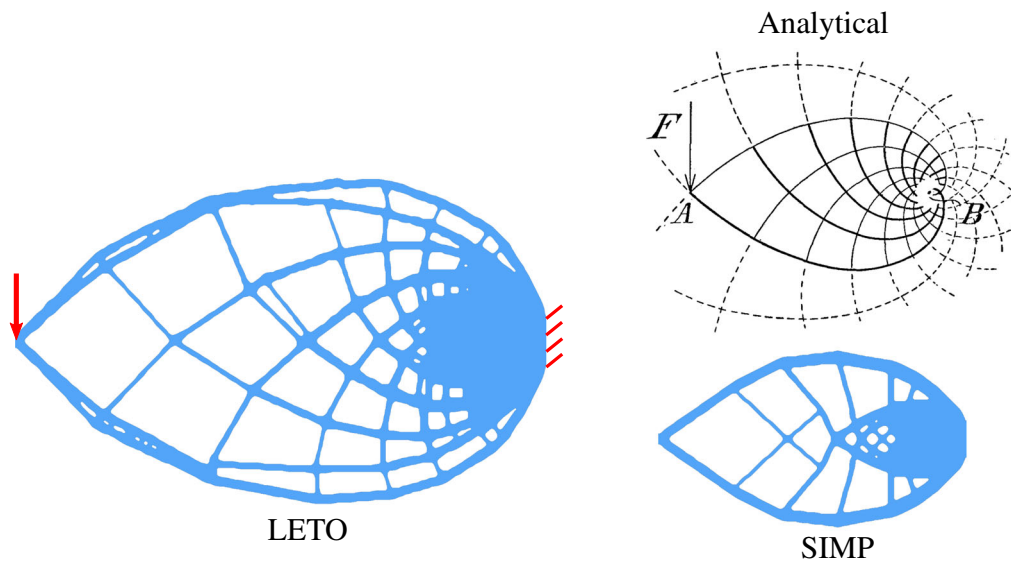


FIGURE 10 Michell truss. Here the resulting structure of Lagrangian–Eulerian topology optimization (LETO) and Solid Isotropic Material with Penalization Method (SIMP) for Michell Truss is evaluated. The central region of the right-most grid is fixed, and a concentrated force is applied in the middle of the leftmost grid. The compliance value evaluated at double-refined grid resolution for LETO and SIMP is 5.054×10^{-2} and 5.055×10^{-2} , respectively. The analytical solution⁷⁸ is shown for reference, albeit the compliance value of both methods are not significantly different, the fiber directions from the proposed method align with those appeared in the analytical solution better

4.2.3 | 2D beam with a distributed load

In this example, the proposed version of LETO and LETO without narrow-band filter (simulate with weak material filling across the whole domain) are also compared to demonstrate the capability of the proposed narrow-band mechanism to remove QR patterns; see Figure 11. To enforce binary design when threshold-increasing narrow-band filter is absent, a family of density mapping functions are used like Heaviside projection in SIMP, except that the functions are smoothly clamped at 0 and 1 to have zero gradient:

$$\hat{\rho}_k(\tilde{\rho}) = \begin{cases} \frac{1}{2}(2\tilde{\rho})^k, & 0 \leq \tilde{\rho} < \frac{1}{2} \\ 1 - \frac{1}{2}(2 - 2\tilde{\rho})^k, & \frac{1}{2} < \tilde{\rho} < 1 \\ 1, & \tilde{\rho} \geq 1, \end{cases} \quad (38)$$

where k is gradually increased from 1.01 to 10 during the optimization.

The design domain is a 4 m × 1 m rectangle. The left boundary is fixed and a total force of 4 N is evenly distributed on the top boundary. The grid resolution is 400 × 100 with a spacing 0.01 m. The target volume is 40%. As highlighted by red boxes, a lot of isolated material blobs form when LETO is used without the narrow-band filter. Such visually isolated material blobs actually belong to one continuum at the simulation resolution but are disconnected at quadrature level (or higher resolution). The large compliance difference between evaluations at low resolution ($c = 6.016 \times 10^{-2}$) and high resolution ($c = 7.804 \times 10^{-3}$) also indicates the inconsistency, which differ by an order of magnitude. The proposed version of LETO can remove those isolated blobs automatically during the optimization, resulting in consistent compliance values when evaluated at optimization resolution $c = 7.845 \times 10^{-3}$ and double resolution ($c = 8.386 \times 10^{-3}$). The compliance of SIMP at double resolution is 1.658×10^{-2} . The final volume reached by SIMP and LETO is 40.0% and 39.7%. Results generated by LETO contains richer intricate fibers than the one by SIMP.

4.2.4 | 3D Beam

Here LETO is further evaluated on a 3D beam problem; see Figure 12. In this example, the design domain is a cuboid of 1.6 m × 0.8 m × 0.8 m. One end of this cubic domain is fixed and a total force of 0.825 N evenly distributes on the bottom edge of the opposite end. A symmetric boundary condition is utilized to reduce the simulation domain to half to save computational cost. The actual simulation grid resolution is 64 × 32 × 16 with a spacing of 0.025 m. The target volume prescription is 20%. With LETO, the result forms a set of thin supporting structures. The compliance for SIMP evaluated at double resolution, LETO evaluated at optimization resolution, and double resolution are 3.527×10^{-4} , 3.323×10^{-4} , 3.334×10^{-4} respectively. The final volume reached by SIMP and LETO is 20.0% and 19.6%.

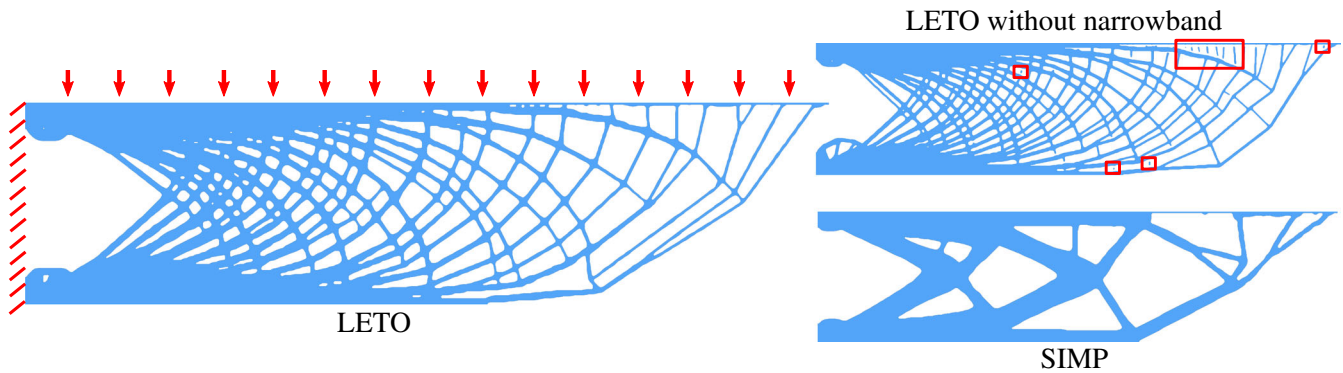


FIGURE 11 Two-dimensional beam with a distributed load. A distributed force load is applied to this beam example at the top plane where the leftmost nodes are fixed. The compliance value evaluated at double-refined grid resolution for Lagrangian–Eulerian topology optimization (LETO) and Solid Isotropic Material with Penalization Method are 8.386×10^{-3} and 1.658×10^{-2} , respectively. LETO without a narrow-band filter is visualized in the top-right corner to demonstrate that the isolated blobs can be removed with the proposed filtering technique

4.2.5 | 3D Bridge

In the second 3D example, LETO is tested on a 3D bridge problem; see Figure 13. The design domain is a cuboid of a length of 4 m, a width of 1 m, and a height of 1 m. The two ending planes along the longest axis are fixed, and a plane force of a total 40.74 N is added on the bottom (denoted by red arrows). Two symmetric boundary conditions are utilized to reduce the simulation domain to a quarter. The grid resolution in optimization is $160 \times 40 \times 40$ with a spacing of 0.025 m. The target volume is 20%. The appearance of LETO and SIMP appears to be significantly different in this example, where LETO generates truss structures with rich fibers in the middle. The compliance value for SIMP evaluated at double resolution, LETO evaluated at optimization resolution, and double resolution are 1.892×10^{-2} , 1.653×10^{-2} , 1.643×10^{-2} , respectively. The final volume reached by SIMP and LETO at double resolution grid are 20.0% and 19.4%.

4.2.6 | Ablation studies

In this section, an ablation study on LETO with different quadrature point distributions, together with a comparison between LETO and SIMP with 1.2 filter radius are demonstrated.

First, two different variations of LETO are compared with the proposed one:

- **LETO with Gaussian quadratures.** The quadratures within each cell are moved to Gaussian points. This means the sample points of the density field are not uniformly distributed as well.

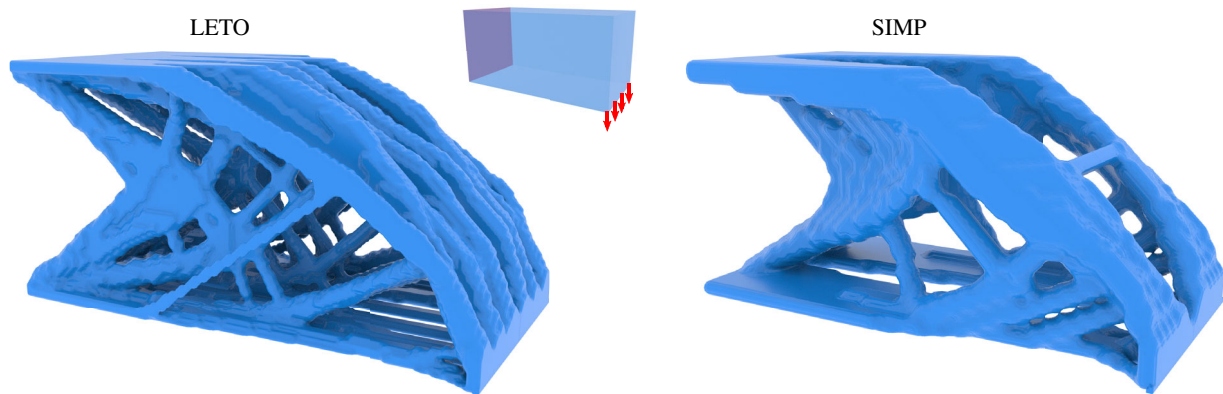


FIGURE 12 Three-dimensional (3D) beam. The results of Solid Isotropic Material with Penalization Method (SIMP) and the proposed method Lagrangian–Eulerian topology optimization (LETO) for this 3D beam example is evaluated. One ending plane of this cubic domain is fixed and forces are applied at the opposite plane's bottom edge. The compliance value evaluated at double-resolution grid for LETO and SIMP is 3.334×10^{-4} , 3.527×10^{-4} , respectively. Richer thin supporting fibers can be seen in the result from the LETO

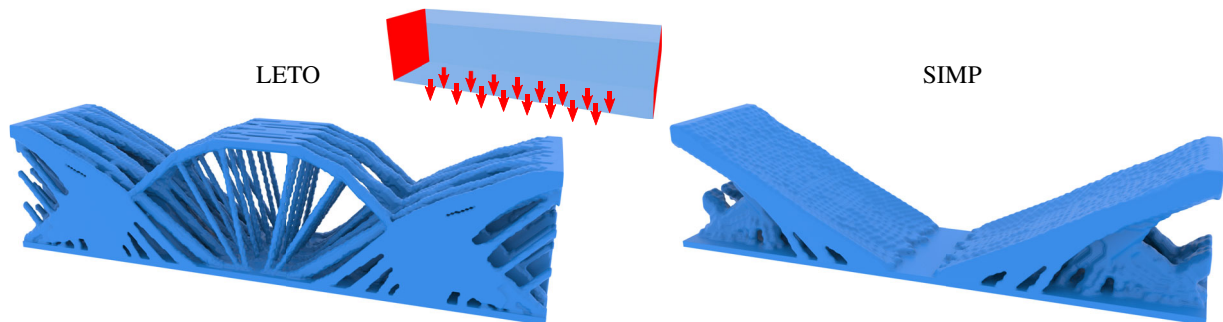


FIGURE 13 Three-dimensional (3D) bridge. A 3D bridge design is considered in this example, where the two ending planes of the cubic design domain is fixed, and a plane force is applied at the bottom. The compliance value evaluated at double-refined grid resolution for Lagrangian–Eulerian topology optimization (LETO) and Solid Isotropic Material with Penalization Method (SIMP) is 1.643×10^{-2} , 1.892×10^{-2} , respectively. LETO produces intricate supporting truss structures unseen in the results from the SIMP method

- **Single-density LETO.** The density field within each cell is a constant. The enforcement is achieved by setting each cell's density as the average density of the uniformly distributed quadratures within that cell. When computing the density field, Gaussian quadratures are utilized to increase the numerical accuracy.

The experiment setup up is the same as Section 4.2.1. The optimization results are shown in Figure 14, where the top-left one is from the proposed LETO. The top-right one and the bottom-left one are from the two variations of LETO. The bottom right one is from SIMP. The quantitative comparison is included in Table 2.

Among these versions of LETO, the proposed one (LETO with uniformly distributed quadratures) performs the best. Compared to uniformly distributed quadratures, Gaussian quadratures may cause bias on the sampling of the density field during the C2P transfer. The quantitative comparison also shows the advantage of uniformly distributed quadratures. The uni-density version of LETO performs worst on this example. However, a notable distinction between the result from uni-density LETO and the result from SIMP is that the result from uni-density LETO has far more fine structures than SIMP. Likewise, the result from the proposed LETO has more fine structures than uni-density LETO. These comparisons show that the multidensity quadrature system and the particle-based material representation jointly contributes to the generated fine structures.

Then LETO is also compared with SIMP with filter radius 1.2. In this case, the filter only touches the adjacent cells on three axes. The results of SIMP on the five linear topology optimization examples are shown in Figure 15. The quantitative comparisons are shown in Table 3. LETO still performs better in these examples and generate finer structures. In addition, 3D results from SIMP have checkerboard artifacts because of the small filter radius.

4.3 | Nonlinear topology optimization

In this section, the robustness of LETO's nonlinear static equilibrium solver is illustrated by varying the force magnitude in large ranges. Two different objectives are also compared: the elastic potential energy and mean compliance $u^T f^{\text{ext}}$,

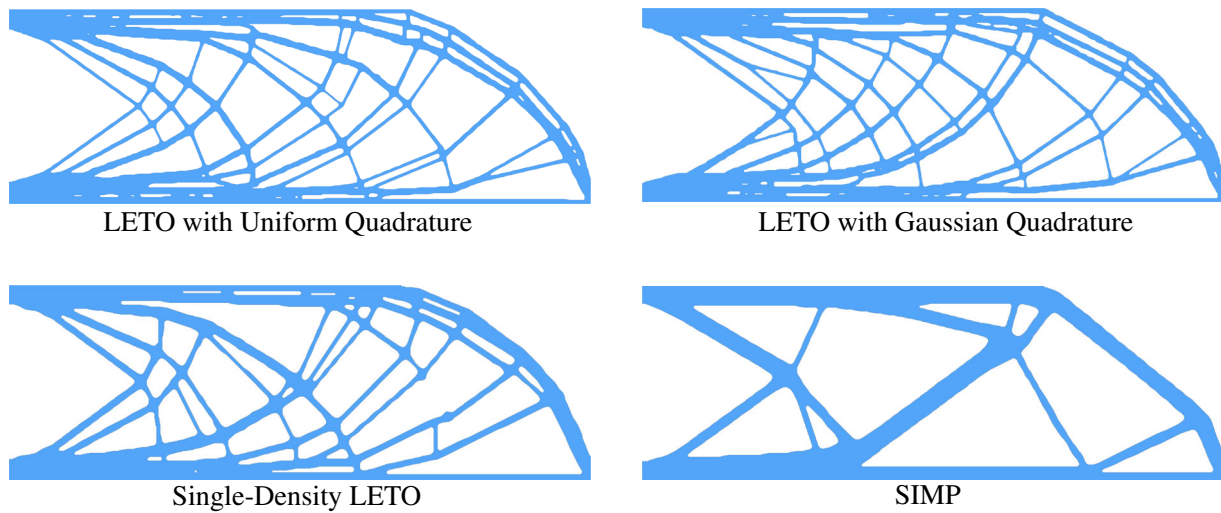


FIGURE 14 Ablation study on variations of Lagrangian-Eulerian topology optimization

TABLE 2 Quantitative comparison between variations of the proposed Lagrangian-Eulerian topology optimization (LETO)

Method	Quadrature system	Constant density in cell	Compliance (refined grid)	Volume
LETO	Uniform	False	1.241×10^{-3}	30.1%
LETO	Gaussian	False	1.257×10^{-3}	30.2%
LETO	Gaussian	True	1.408×10^{-3}	30.5%
SIMP	Gaussian	True	1.264×10^{-3}	30.1%

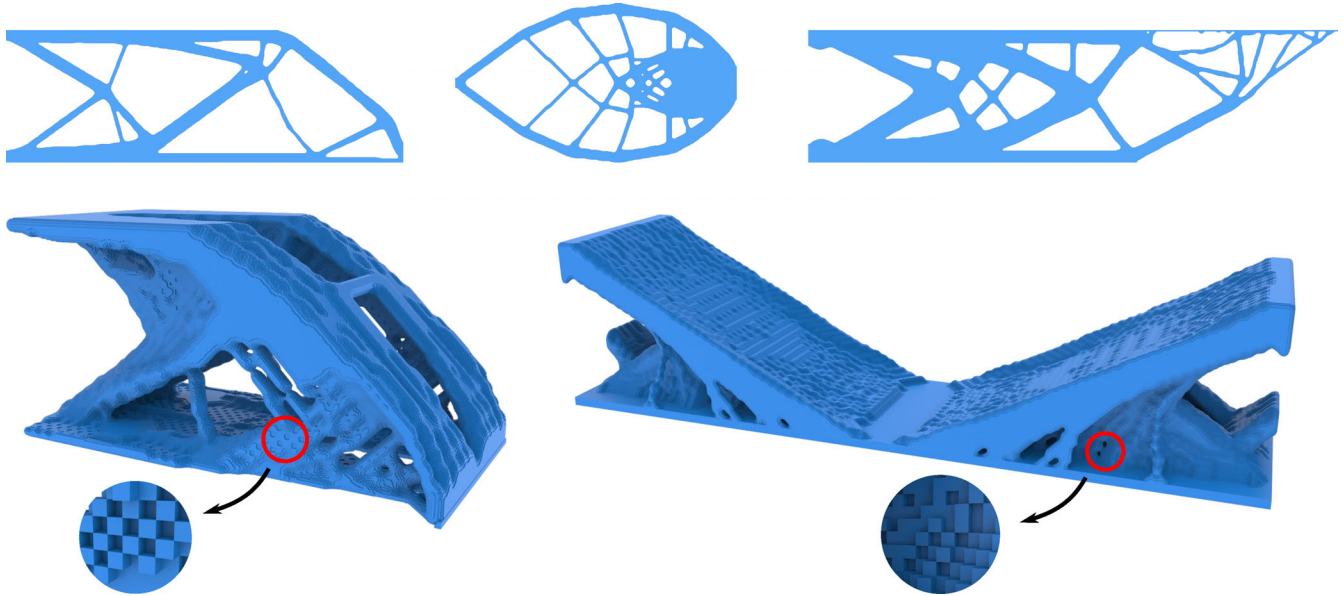


FIGURE 15 Linear topology optimization results of Solid Isotropic Material with Penalization with filter radius 1.2

Experiment	LETO		SIMP (filter radius = 1.2)	
	Compliance (refined grid)	Volume	Compliance (refined grid)	Volume
Concentrated-load beam	1.243×10^{-3}	29.9%	1.316×10^{-3}	30.0%
Michell truss	5.054×10^{-2}	20.1%	5.055×10^{-2}	20.1%
Distributed-load beam	8.386×10^{-3}	39.7%	1.458×10^{-2}	40.0%
3D beam	3.334×10^{-4}	19.6%	3.666×10^{-4}	20.0%
3D bridge	1.643×10^{-2}	19.4%	1.938×10^{-2}	20.0%

TABLE 3 Quantitative comparison between Lagrangian–Eulerian topology optimization (LETO) and Solid Isotropic Material with Penalization Method (SIMP) with filter radius 1.2

where f^{ext} is the nodal external force field and u is the nodal displacement field. Many topology optimization methods for nonlinear elasticity only consider cases with small strains, thus utilize the mean compliance as the objective function, essentially a linearization of the elastic potential.^{26,79,80} The two objectives are equivalent in linear elasticity up to a factor. The following examples show that they differ significantly under large force magnitude. Minimizing the mean compliance is equivalent to minimizing the displacements at force loading points. However, that does not necessarily minimize the elastic energy stored in the material. Buckled structures will appear to reduce potential energy when force magnitude is large. The examples shown are all optimized with nonlinear LETO. The compliance and mean compliance value reported are all evaluated on a double refined grid as in the linear topology optimization examples.

4.3.1 | 2D Long beam

In this example, a concentrated force is applied at the bottom center of a long beam; see Figure 16. The $4 \text{ m} \times 1 \text{ m}$ design domain is discretized with a grid resolution 800×100 . The target volume is 20%. Force magnitude at 1, 10, 50, 100 N are tested. As shown in Figure 16, when the force magnitude is small, the result is close to that of linear topology optimization. As the force becomes larger, more and more fibers form between the force port and the two top corners. And finally, a lot of buckled fibers appear.

Under the maximal tested force magnitude, results of compliance (elastic potential energy) minimization and mean compliance minimization are compared; see Figure 17. The undeformed and deformed states are differentiated by translucent and solid coloring. The final compliance of the result by minimizing elastic potential is 3.473 and the mean compliance of the result by minimizing mean compliance is 3.921. Although the displacement of force port is much

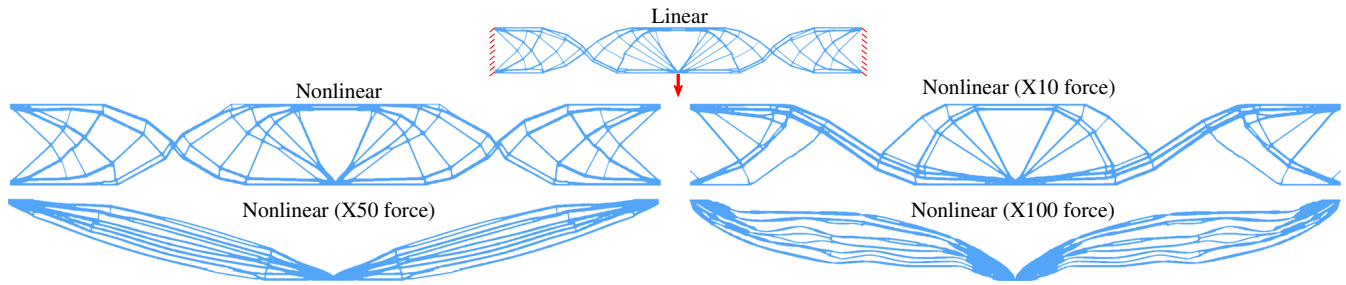


FIGURE 16 Two-dimensional long beam. The results of the proposed method under different force magnitudes are shown in this figure. The resulting material distribution differs sharply and a clear buckling behavior manifested. It can be seen that the proposed method is robust under large deformations

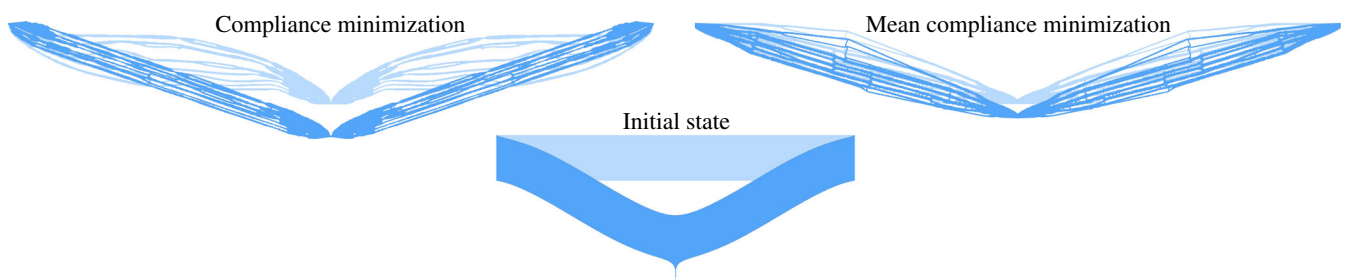
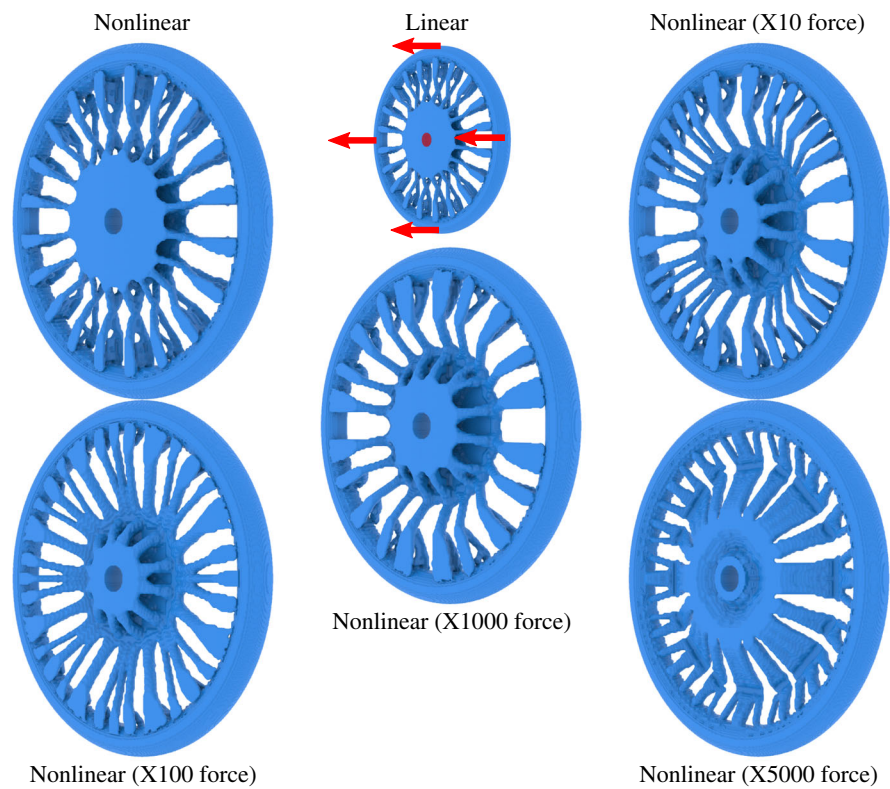


FIGURE 17 Two-dimensional long beam structure with different objectives. The resulting material distribution of minimizing compliance and mean compliance under $\times 100$ force is shown in this figure

FIGURE 18 Three-dimensional (3D) wheel. In this example, a large range of force magnitudes is tested to further examine the robustness of the proposed method in 3D. Out-of-plane forces are applied to the wheel and the central region is fixed



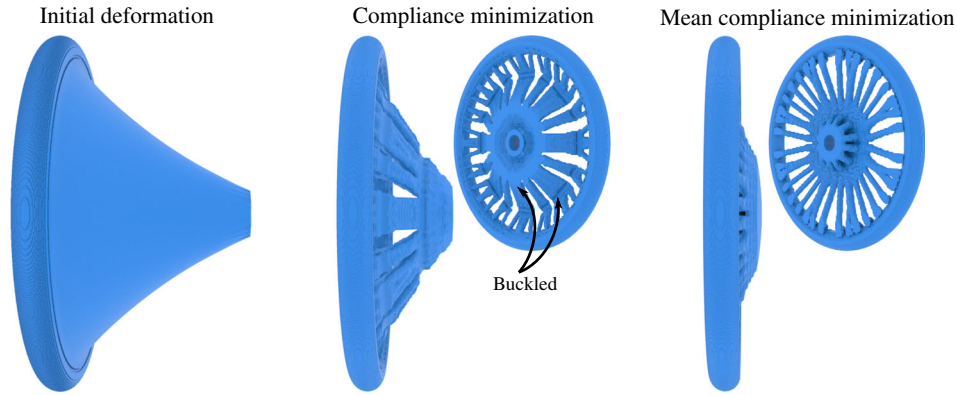


FIGURE 19 Three-dimensional wheel structure with different objectives. The difference in considering compliance and mean compliance as the objective function is further compared in this experiment, where a force is enforced to create significantly large initial deformation. Minimizing compliance objective delivers strong buckling behavior in the resulting structure

smaller when minimizing mean compliance, the elastic energy stored in the structure is much larger: the compliance of the result by minimizing mean compliance is 8.535, which is significantly larger than the compliance value resulting from minimizing the elastic potential.

4.3.2 | 3D Wheel

In this example, LETO is tested on a 3D wheel design problem under normal forces; see Figure 18. The design domain is a flat cylinder bounded by a torus. The outer radius and inner radius of the torus are 1.2 and 1 m, respectively. The grid resolution is $96 \times 96 \times 8$ with spacing 0.025 m. A small cylinder through the center of the wheel is fixed, and the outer torus is set to maintain solid. Forces are perpendicular to the wheel plane and are evenly exerted on a thin layer of the wheel's outer-most boundary. The magnitude of total force at 1.09×10^{-2} , 1.09×10^{-1} , 1.09 , 1.09×10^1 , 5.44×10^1 N are tested. The target volume is 20%. When the force magnitude is small, the result of nonlinear elasticity is almost identical to linear elasticity, which is symmetric w.r.t. the wheel plane. As the force magnitude becomes larger, the symmetry disappears, and the spokes become denser.

Same as the 2D example, when the force is very large, buckled fibers appear. As shown in Figure 19, the buckled spokes open up in the deformed state. Result optimized by minimizing mean compliance is shown as well to compare. Although the overall deformation of it appears to be more moderate than the compliance-minimized result, it actually stores significantly more energy. The mean compliance of the mean-compliance-minimized result is 2.946. However, the energy it contains is 6.960, while the compliance of the compliance-minimized result is only 2.063.

5 | CONCLUSION AND FUTURE WORK

A new hybrid LETO method is proposed. MPM discretization is used to enable subcell resolution on the fly. The method produces intricate results with comparable and sometimes lower compliance at similar simulation costs than Eulerian methods. With a unified treatment, the proposed method optimizes the elastic potential as the compliance objective for both linear and highly nonlinear (e.g., neo-Hookean) hyperelastic materials. Notably, the method robustly captures large deformation and buckling behaviors in nonlinear cases.

The finite strain formulation in MPM allows the construction of a unified framework for general hyperelastic materials. With the ability to resolve subcell features, LETO can be further extended in future work to optimize anisotropic, heterogeneous, and multiscale materials. It would also be interesting to apply this framework to optimize different objectives, for example, compliant mechanisms and task-oriented objectives for designing soft robots.

In the 2D long-beam example for nonlinear elasticity, slight overlaps between some fibers happen under the maximal tested load when the equilibrium is solved with the narrow-band filter turned on. However, when the equilibrium is solved with weak material like SIMP, the noninvertible neo-Hookean constitutive model will push fibers apart. This brings the inspiration that noninvertible weak material could be a contact handling model. On the other hand, it is tricky

to tune weak material's Young's modulus—too large Young's modulus can provide nonrealistic supporting force. On the other hand, too small Young's modulus may cause numerical issues, not to mention that the weak material wastes a lot of computational power. More robust handling of contact should be developed to enable contact-aware topology optimization.

Last but not least, the method relies on MMA. As mentioned, MMA requires careful parameter tuning to perform well. Even with the general and consistent regularizations for all examples on step length and the relative scaling between constraints and objective, it is still unclear whether the optimization parameters chosen in this paper are optimal. It is also unclear whether the current MMA parameters can conveniently adapt for extensions to more complex materials. Therefore, it would be meaningful to develop a more general and easy-to-setup optimizer, likely taking advantage of second-order design sensitivity information.

ACKNOWLEDGEMENTS

This work was supported in part by NSF CAREER IIS-1943199, CCF-1813624, ECCS-2023780, MRI-19196, ONR MURI N00014-16-12007, ONR N00014-19-1-2153, DARPA XAI N66001-17-2-4029, Dartmouth Neukom Institute CompX Faculty Grant, Burke Research Initiation Award, and Toyota Motor Engineering & Manufacturing North America.

DATA AVAILABILITY STATEMENT

The data that support the findings of this study are available from the corresponding author upon request.

ORCID

Xuan Li  <https://orcid.org/0000-0003-0677-8369>

REFERENCES

1. Aage N, Andreassen E, Lazarov BS, Sigmund O. Giga-voxel computational morphogenesis for structural design. *Nature*. 2017;550(7674):84.
2. Liu H, Hu Y, Zhu B, Matusik W, Sifakis E. Narrow-band topology optimization on a sparsely populated grid. *SIGGRAPH Asia*. Vol 2018. New York, NY: ACM; 2018:251.
3. Wu J, Dick C, Westermann R. A system for high-resolution topology optimization. *IEEE Trans Vis Comput Graph*. 2015;22(3):1195-1208.
4. Sigmund O. A 99 line topology optimization code written in Matlab. *Struct Multidiscip Optim*. 2001;21(2):120-127.
5. Andreassen E, Clausen A, Schevenels M, Lazarov BS, Sigmund O. Efficient topology optimization in MATLAB using 88 lines of code. *Struct Multidiscip Optim*. 2011;43(1):1-16.
6. Osher S, Sethian JA. Fronts propagating with curvature-dependent speed: algorithms based on Hamilton-Jacobi formulations. *J Comput Phys*. 1988;79(1):12-49.
7. Wang MY, Wang X, Guo D. A level set method for structural topology optimization. *Comput Methods Appl Mech Eng*. 2003;192(1-2):227-246.
8. Allaire G, Jouve F, Toader AM. Structural optimization using sensitivity analysis and a level-set method. *J Comput Phys*. 2004;194(1):363-393.
9. Luo Z, Wang MY, Wang S, Wei P. A level set-based parameterization method for structural shape and topology optimization. *Int J Numer Methods Eng*. 2008;76(1):1-26.
10. Van Dijk NP, Maute K, Langelaar M, Van Keulen F. Level-set methods for structural topology optimization: a review. *Struct Multidiscip Optim*. 2013;48(3):437-472.
11. Gingold RA, Monaghan JJ. Smoothed particle hydrodynamics: theory and application to non-spherical stars. *Mon Not R Astron Soc*. 1977;181(3):375-389.
12. Christiansen AN, Nobel-Jørgensen M, Aage N, Sigmund O, Bærentzen JA. Topology optimization using an explicit interface representation. *Struct Multidiscip Optim*. 2014;49(3):387-399.
13. Harlow FH. The particle-in-cell method for numerical solution of problems in fluid dynamics. Technical report, Los Alamos Scientific Lab: 1962.
14. Brackbill JU, Kothe DB, Ruppel HM. FLIP: a low-dissipation, particle-in-cell method for fluid flow. *Comput Phys Commun*. 1988;48(1):25-38.
15. Sulsky D, Zhou SJ, Schreyer HL. Application of a particle-in-cell method to solid mechanics. *Comput Phys Commun*. 1995;87(1-2):236-252.
16. de Vaucorbeil A, Nguyen VP, Sinaie S, Wu JY. Material point method after 25 years: Theory, implementation, and applications. *Advances in Applied Mechanics*; Amsterdam, Netherlands: Elsevier; 2020.
17. Zhang X, Chen Z, Liu Y. *The Material Point Method: A Continuum-Based Particle Method for Extreme Loading Cases*. Cambridge, Massachusetts, USA: Academic Press; 2016.
18. Guo X, Zhang W, Zhong W. Doing topology optimization explicitly and geometrically—a new moving morphable components based framework. *J Appl Mech*. 2014;81(8):081009.
19. Zhang W, Zhang J, Guo X. Lagrangian description based topology optimization—a revival of shape optimization. *J Appl Mech*. 2016;83(4):041010.

20. Zhang W, Chen J, Zhu X, et al. Explicit three dimensional topology optimization via Moving Morphable Void (MMV) approach. *Comput Methods Appl Mech Eng*. 2017;322:590-614.
21. Zhang W, Song J, Zhou J, et al. Topology optimization with multiple materials via moving morphable component (MMC) method. *Int J Numer Methods Eng*. 2017;113(11):1653-1675. <https://doi.org/10.1002/nme.5714>.
22. Zhang W, Li D, Yuan J, Song J, Guo X. A new three-dimensional topology optimization method based on moving morphable components (MMCs). *Comput Mech*. 2017;59(4):647-665.
23. Lei X, Liu C, Du Z, Zhang W, Guo X. Machine learning-driven real-time topology optimization under moving morphable component-based framework. *J Appl Mech*. 2019;86(1):011004-011012.
24. Zhang W, Li D, Zhang J, Guo X. Minimum length scale control in structural topology optimization based on the Moving Morphable Components (MMC) approach. *Comput Methods Appl Mech Eng*. 2016;311:327-355. <https://doi.org/10.1016/j.cma.2016.08.022>.
25. Overvelde JT. *The Moving Node Approach in Topology Optimization* [PhD thesis]. Delft University of Technology; 2012.
26. Buhl T, Pedersen CB, Sigmund O. Stiffness design of geometrically nonlinear structures using topology optimization. *Struct Multidiscip Optim*. 2000;19(2):93-104.
27. Maute K, Sigmund O. Topology optimization approaches: a comparative review. *Struct Multidiscip Optim*. 2013;48(6):1031-1055.
28. Stomakhin A, Schroeder C, Chai L, Teran J, Selle A. A material point method for snow simulation. *ACM Trans Graph (TOG)*. 2013;32(4):102.
29. Wolper J, Fang Y, Li M, Lu J, Gao M, Jiang C. CD-MPM: Continuum damage material point methods for dynamic fracture animation. *ACM Trans Graph (TOG)*. 2019;38(4):119.
30. Abe K, Soga K, Bandara S. Material point method for coupled hydromechanical problems. *J Geotech Geoenviron*. 2014;140(3):04013033.
31. Zabala F, Alonso E. Progressive failure of Aznalcóllar dam using the material point method. *Géotechnique*. 2011;61(9):795-808.
32. Guilkey JE, Weiss JA. Implicit time integration for the material point method: quantitative and algorithmic comparisons with the finite element method. *Int J Numer Methods Eng*. 2003;57(9):1323-1338.
33. Sinaie S, Ngo TD, Nguyen VP, Rabczuk T. Validation of the material point method for the simulation of thin-walled tubes under lateral compression. *Thin-Walled Struct*. 2018;130:32-46.
34. Chen Z, Brannon R. An evaluation of the material point method. SAND Report, SAND2002-0482,(February 2002); 2002.
35. Nair A, Roy S. Implicit time integration in the generalized interpolation material point method for finite deformation hyperelasticity. *Mech Adv Mater Struct*. 2012;19(6):465-473.
36. Charlton T, Coombs W, iGIMP AC. An implicit generalised interpolation material point method for large deformations. *Comp Struct*. 2017;190:108-125.
37. Nguyen VP, Nguyen GDA. Voronoi cell material point method for large deformation solid mechanics problems. *Applied Mechanics and Materials*. Vol 846. Stafa-Zurich, Switzerland: Trans Tech Publications; 2016:108-113.
38. Sadeghirad A, Brannon RM, Burghardt J. A convected particle domain interpolation technique to extend applicability of the material point method for problems involving massive deformations. *Int J Numer Methods Eng*. 2011;86(12):1435-1456.
39. Soga K, Alonso E, Yerro A, Kumar K, Bandara S. Trends in large-deformation analysis of landslide mass movements with particular emphasis on the material point method. *Géotechnique*. 2016;66(3):248-273.
40. Lian Y, Zhang X, Liu Y. An adaptive finite element material point method and its application in extreme deformation problems. *Comput Methods Appl Mech Eng*. 2012;241:275-285.
41. Guo Y, Nairn J. Three-dimensional dynamic fracture analysis using the material point method. *Comput Model Eng Sci*. 2006;16(3):141.
42. Yang P, Gan Y, Zhang X, Chen Z, Qi W, Liu P. Improved decohesion modeling with the material point method for simulating crack evolution. *Int J Fract*. 2014;186(1-2):177-184.
43. Long CC, Moutsanidis G. *Using a Single Velocity Field within the Material Point Method to Model Fracture and Multi-Body Interactions*. Technical Report. Los Alamos, NM: Los Alamos National Lab.(LANL); 2019.
44. Long C, Zhang D, Bronkhorst C, Gray IIIG. Representing ductile damage with the dual domain material point method. *Comput Methods Appl Mech Eng*. 2016;300:611-627.
45. Homel MA, Herbold EB. Field-gradient partitioning for fracture and frictional contact in the material point method. *Int J Numer Methods Eng*. 2017;109(7):1013-1044.
46. Fang Y, Li M, Gao M, Jiang C. Silly rubber: an implicit material point method for simulating non-equilibrated viscoelastic and elastoplastic solids. *ACM Trans Graph (TOG)*. 2019;38(4):118.
47. Burghardt J, Brannon R, Guilkey J. A nonlocal plasticity formulation for the material point method. *Comput Methods Appl Mech Eng*. 2012;225:55-64.
48. Kularathna S, Soga K. Implicit formulation of material point method for analysis of incompressible materials. *Comput Methods Appl Mech Eng*. 2017;313:673-686.
49. Zhang F, Zhang X, Sze KY, Lian Y, Liu Y. Incompressible material point method for free surface flow. *J Comput Phys*. 2017;330:92-110.
50. Ma S, Zhang X, Lian Y, Zhou X. Simulation of high explosive explosion using adaptive material point method. *Comput Model Eng Sci (CMES)*. 2009;39(2):101.
51. Gaume J, Gast T, Teran J, Van Herwijnen A, Jiang C. Dynamic anticrack propagation in snow. *Nature Commun*. 2018;9(1):1-10.
52. Gaume J, van Herwijnen A, Gast T, Teran J, Jiang C. Investigating the release and flow of snow avalanches at the slope-scale using a unified model based on the material point method. *Cold Reg Sci Technol*. 2019;168:102847.
53. Bardenhagen S, Brackbill J, Sulsky D. The material-point method for granular materials. *Comput Methods Appl Mech Eng*. 2000;187(3-4):529-541.

54. Klár G, Gast T, Pradhana A, et al. Drucker-prager elastoplasticity for sand animation. *ACM Trans Graph (TOG)*. 2016;35(4):103.
55. Yerro A, Soga K, Bray J. Runout evaluation of Oso landslide with the material point method. *Can Geotech J*. 2019;56(9):1304-1317.
56. Zhang H, Wang K, Chen Z. Material point method for dynamic analysis of saturated porous media under external contact/impact of solid bodies. *Comput Methods Appl Mech Eng*. 2009;198(17-20):1456-1472.
57. Gao M, Pradhana A, Han X, et al. Animating fluid sediment mixture in particle-laden flows. *ACM Trans Graph (TOG)*. 2018;37(4):1-11.
58. Tampubolon AP, Gast T, Klár G, et al. Multi-species simulation of porous sand and water mixtures. *ACM Trans Graph (TOG)*. 2017;36(4):105.
59. Bandara S, Soga K. Coupling of soil deformation and pore fluid flow using material point method. *Comput Geotech*. 2015;63:199-214.
60. Steffen M, Kirby R, Berzins M. Analysis and reduction of quadrature errors in the material point method (MPM). *Int J Numer Methods Eng*. 2008;76(6):922-948.
61. Wallstedt P. *On the Order of Accuracy of the Generalized Interpolation Material Point Method*. Salt Lake City, UT, United States: University of Utah; 2009.
62. Scharff RB, Wu J, Geraedts JM, Wang CC. Reducing out-of-plane deformation of soft robotic actuators for stable grasping. Paper presented at: Proceedings of the 2019 2nd IEEE International Conference on Soft Robotics (RoboSoft), Seoul, Korea (South); 2019; IEEE.
63. Batty C, Bertails F, Bridson R. A fast variational framework for accurate solid-fluid coupling. *ACM Trans Graph (TOG)*. 2007;26(3):100-es.
64. Gast TF, Schroeder C, Stomakhin A, Jiang C, Teran JM. Optimization integrator for large time steps. *IEEE Trans Vis Comput Graph (TVCG)*. 2015;21(10):1103-1115.
65. Wang X, Li M, Fang Y, et al. Hierarchical optimization time integration for CFL-rate MPM stepping; 2019; arXiv preprint arXiv:1911.07913.
66. Liu T, Bouaziz S, Kavan L. Quasi-newton methods for real-time simulation of hyperelastic materials. *ACM Trans Graph (TOG)*. 2017;36(3):1-16.
67. Smith B, Goes FD, Kim T. Stable neo-hookean flesh simulation. *ACM Trans Graph (TOG)*. 2018;37(2):1-15.
68. Teran J, Sifakis E, Irving G, Fedkiw R. Robust quasistatic finite elements and flesh simulation. Paper presented at: Proceedings of the 2005 ACM SIGGRAPH/Eurographics Symposium on Computer Animation (SCA); 2005:181-190; ACM, New York, NY.
69. Nguyen TH, Paulino GH, Song J, Le CH. A computational paradigm for multiresolution topology optimization (MTOP). *Struct Multidiscip Optim*. 2009;41(4):525-539. <https://doi.org/10.1007/s00158-009-0443-8>.
70. Gupta DK, Langelaar M, vF K. QR-patterns: artefacts in multiresolution topology optimization. *Struct Multidiscip Optim*. 2018;58(4):1335-1350. <https://doi.org/10.1007/s00158-018-2048-6>.
71. Groen JP, Langelaar M, Sigmund O, Ruess M. Higher-order multi-resolution topology optimization using the finite cell method. *Int J Numer Methods Eng*. 2016;110(10):903-920. <https://doi.org/10.1002/nme.5432>.
72. Giles MB, Pierce NA. An introduction to the adjoint approach to design. *Flow Turbul Combust*. 2000;65(3-4):393-415.
73. Nocedal J, Wright S. *Numerical Optimization*. Berlin, Germany: Springer Science & Business Media; 2006.
74. Svanberg K. The method of moving asymptotes—a new method for structural optimization. *Int J Numer Methods Eng*. 1987;24(2):359-373.
75. de Vaucorbeil A, Nguyen VP, Hutchinson CR. A total-Lagrangian material point method for solid mechanics problems involving large deformations. *Comput Methods Appl Mech Eng*. 2020;360:112783.
76. Smith J, Schaefer S. Bijective parameterization with free boundaries. *ACM Trans Graph (TOG)*. 2015;34(4):1-9.
77. Guest JK, Prévost JH, Belytschko T. Achieving minimum length scale in topology optimization using nodal design variables and projection functions. *Int J Numer Methods Eng*. 2004;61(2):238-254.
78. Michell A. LVIII: the limits of economy of material in frame-structures. *Lond Edinburgh Dublin Philos Mag J Sci*. 1904;8(47):589-597. <https://doi.org/10.1080/14786440409463229>.
79. Bruns T, Tortorelli D. *Topology Optimization of Geometrically Nonlinear Structures and Compliant Mechanisms*. Reston, VA, United States: American Institute of Aeronautics and Astronautics; 1998.
80. Gea HC, Luo J. Topology optimization of structures with geometrical nonlinearities. *Comput Struct*. 2001;79(20-21):1977-1985.

How to cite this article: Li Y, Li X, Li M, Zhu Y, Zhu B, Jiang C. Lagrangian–Eulerian multidensity topology optimization with the material point method. *Int J Numer Methods Eng*. 2021;1–25. <https://doi.org/10.1002/nme.6668>